Multistatic Scatter Radio Sensor Networks for Extended Coverage

Panos N. Alevizos, *Student Member, IEEE*, Konstantinos Tountas, *Student Member, IEEE*, and Aggelos Bletsas, *Senior Member, IEEE*

***Abstract*— Scatter radio, i.e., communication by means of reflection, has been recently proposed as a viable ultra-low power solution for wireless sensor networks (WSNs). This paper offers a detailed comparison between monostatic and multistatic scatter radio architectures. In monostatic architecture, the reader consists of both the illuminating transmitter and the receiver of signals scattered back from the sensors. The multistatic architecture includes several ultra-low cost illuminating carrier emitters and a single reader. Maximum-likelihood coherent and noncoherent bit error rate (BER), diversity order, average information, and energy outage probability comparison is performed, under dyadic Nakagami fading and filling a gap in the literature. It is found that: 1) diversity order, BER, and tag location-independent performance bounds of multistatic architecture outperform monostatic; 2) energy outage due to radio frequency (RF) harvesting for passive tags, is less frequent in multistatic than monostatic architecture; and 3) multistatic coverage is higher than monostatic. Furthermore, a proof-of-concept digital multistatic scatter radio WSN with a single receiver, four low-cost emitters, and multiple ambiently-powered low-bitrate tags, perhaps the first of its kind, is experimentally demonstrated (at 13 dBm transmission power), covering an area of 3500 m^2. Research findings are applicable in the industries of WSNs, RF identification, and emerging Internet-of-Things.**

***Index Terms*— Multiple access interference, Nakagami channels, scattering parameters, radio frequency wireless sensor networks.**

I. Introduction

TYPICAL wireless sensor networks (WSNs) utilize conventional (Marconi) radios for communication. Such radio frequency (RF) front-ends typically require signal conditioning units, such as mixers, active filters, and amplifiers, increasing complexity, power consumption, and cost. On the other hand, scatter radio, i.e., communication by means of reflection, has been recently proposed as a viable ultra-low power solution for WSNs [1]. Scattering can be achieved with a single RF transistor at each scatter radio node (called tag henceforth), significantly reducing power and monetary cost per WSN terminal. Scatter radio has been exploited in various interfaces [2], [3] and radio frequency identification (RFID), widely used for inventorying, electronic tickets, and people identification [4], [5]; it is also expected to play a key role in the evolution of Internet-of-Things (IoT) and related applications [6], [7].

In environmental monitoring and precision agriculture, the tag/sensors must cover an extended area and thus, link ranges between the tags and the interrogator (*reader*) must be maximized. There are two different architectures for scatter radio networks: the monostatic and the multi-bistatic (multistatic) architectures, depicted in Fig 1. Typical RFID applications utilize the monostatic architecture, along with *passive* tags, i.e., powered by the illuminating field of the transmitting interrogator. In the monostatic architecture, the reader consists of both the illuminating transmitter and the receiver of signals reflected back from the tags. Additionally, passive tags require a rectification circuit to convert the RF signals (captured by the tag antenna) to DC voltage, powering the tag. Thus, the achievable range is limited by the "forward link" [8] and the RF harvesting circuitry. Moreover, commercial tags implement high bitrate communication for the tag-to-reader link, typically in the order of a few hundreds of kilo bits per second, resulting in reduced energy per bit, and thus, limited communication range.

In the bistatic architecture, the illuminating carrier emitter (CE) and the receiver of the reflected (backscattered) signals are distinct units, located at different positions, offering flexible network topologies. In the multistatic architecture, several low-cost CEs are available, two orders of magnitude cheaper than the reader. The latter can be a low-cost, commodity software-defined radio (SDR). Due to the morphology of the multistatic architecture, each tag can be close to a CE with high probability, offering two desired implications: (a) the tag-to-reader coverage is increased with high probability and (b) using passive tags that harvest RF energy from the illuminating emitters, the probability of energy outage during the energy harvesting phase can be decreased.

Work in [1] studied a semi-passive, low-bitrate scatter radio tag, i.e., *energy*-assisted tag (e.g., from battery, low-cost solar

Manuscript received May 30, 2017; revised September 25, 2017 and February 10, 2018; accepted March 31, 2018. Date of publication April 23, 2018; date of current version July 10, 2018. This work was supported by the ERC-04-BLASE project, executed in the context of the "Education & Lifelong Learning" Operational Program of the National Strategic Reference Framework (NSRF), General Secretariat for Research & Technology (GSRT), funded through European Union-European Social Fund and Greek national funds. This paper was presented at the EURFID Workshop, Rosenheim, Germany, October 2015. The associate editor coordinating the review of this paper and approving it for publication was C. R. Anderson.

P. N. Alevizos and A. Bletsas are with the Telecom Laboratory, School of ECE, Technical University of Crete, 73100 Chania, Greece (e-mail: palevizos@isc.tuc.gr; aggelos@telecom.tuc.gr).

K. Tountas is with the Department of Computer and Electrical Engineering and Computer Science, Florida Atlantic University, Boca Raton, FL 33431 USA (e-mail: ktountas2017@fau.edu).

Color versions of one or more of the figures in this paper are available online at http://ieeexplore.ieee.org.

Digital Object Identifier 10.1109/TWC.2018.2827034

panel). The work studied also the relevant signal processing and noncoherent detection algorithms with scatter radio minimum-shift keying (MSK) and monostatic architecture, i.e., with transmitting and receiving antenna at the same, custom reader. Frequency division multiplexing among sensors was possible, due to frequency-shift keying (FSK) and orthogonal modulating scatter radio frequencies among the tags. Subsequent work in [9] studied frequency reuse and adjacent frequency channel interference in cellular architectures, where each cell is served by a different reader and modulating scatter radio (i.e., *subcarrier*) frequencies are reused across different (and distant) cells. Work in [10] and [11] studied link budgets of the general multi-antenna scatter radio link, showing multi-antenna benefits on bit error rate (BER). Coverage analysis for WSNs consisting of passive devices has been conducted in [12] and [13].

Bistatic scatter radio—with emitter and receiver located at different locations, as separate units—was analyzed and experimentally demonstrated in [14]–[16], focusing on noncoherent FSK or on-off keying and highlighting the idiosyncrasies of scatter radio compared to classic, Marconi radio, as well as the additional difficulties imposed by the bistatic architecture (e.g., carrier frequency offset between emitter and receiver). Work in [17] and [18] studied and experimentally demonstrated short packet communication with error correction and proposed specific soft-decision metrics for noncoherent detection in the bistatic scatter radio architecture, while work in [19] offered coherent detection and decoding with short block length channel codes (and short preambles necessary for channel estimation), after carefully compressing all channel and microwave unknowns of the bistatic system to a single complex vector. Coherent detection and SDR-based reception of industrial RFID was shown in [20]. Advanced noncoherent detectors and decoders based on composite hypothesis-testing are proposed in [18] and [21] performing very close to perfect CSI, emphasizing on short packet communication. Scatter radio WSN examples, using, however, analog frequency modulation principles, were given for environmental humidity in [22] and for soil moisture in[23] and [24]. Work in [25] is another example of bistatic scatter radio, where the illuminating signal is the (modulated) digital television (DTV) signal, while work in [26] uses bistatic scatter radio principles to convert Bluetooth transmissions to create Wi-Fi and ZigBee-compatible signals. Detectors for ambient backscatter systems relying on bistatic architecture have been proposed in [27] and [28].

This work proposes multistatic scatter radio WSN architecture for extended coverage and reliability. A detailed comparison methodology between monostatic and multistatic architectures for scatter radio WSNs is offered, examining various performance metrics, such as BER, energy outage probability (in passive tags), and information outage probability. The contributions of this work are summarized as follows:

- A multi-user signal model is offered, based on joint time- and frequency-division multiplexing (joint TDM-FDM) for both multistatic and monostatic systems, exploiting existing results on scatter radio prior art. The signal model accounts for (large-scale) path-loss and small-scale fading, based on dyadic Nakagami fading (which can model a wide class of fading channels, including Rayleigh and Rice).
- Upper bounds on BER performance of point-to-point backscatter systems under coherent maximum-likelihood (ML) detection for dyadic Nakagami fading are derived. These bounds coincide with the exact BER performance of noncoherent envelope detection.
- It is found that the bistatic architecture has higher diversity order than the monostatic architecture. Additionally, the multistatic analysis covers asymmetric cases, where emitter-to-tag and tag-to-reader links follow different fading statistics. The latter is useful in evaluating recently proposed *ambient* scenarios, where scatter radio tag is close to the receiver but distant from the illuminating ambient emitter.
- Information outage probability and tight Jensen-based upper bounds are provided for Rayleigh fading. In addition, for WSNs consisting of passive tags, closed-form expressions for energy outage are derived for Nakagami fading.
- A framework for tag topology-independent outage performance evaluation is offered based on randomization of tags' positions over square grid topologies. Detailed simulation study reveals that the multistatic architecture outperforms the monostatic for every studied performance metric.
- A digital multistatic, scatter radio WSN is experimentally demonstrated and contrasted to a monostatic counterpart, corroborating the theoretical findings and offering a concrete proof-of-concept.

The rest of this document is organized as follows: Section II presents the model of the monostatic and multistatic architectures. Section III presents the single user (i.e., tag) error probability analysis and Section IV offers the outage probability analysis for multiple users. Section V discusses about diversity reception and presents how to model the spatial distribution of tags, while Section VI offers energy information outage analytical results. Numerical and experimental (outdoor) results are presented in Sections VII and VIII, respectively. Finally, work is concluded in Section IX.

Notation: Symbols $\mathbb{B}$, $\mathbb{N}$, $\mathbb{R}$, and $\mathbb{C}$ denote the set of binary, natural, real, and complex numbers, respectively. $\mathbf{0}_N$ and $\mathbf{I}_N$, denote, respectively, the all-zeros vector and identity matrix of size N. The phase of a complex number z is denoted as $\angle z$. The distribution of a proper complex Gaussian $N \times 1$ vector $\mathbf{x}$ with mean $\boldsymbol{\mu}$ and covariance matrix $\boldsymbol{\Sigma}$ is denoted by $\mathcal{CN}(\boldsymbol{\mu}, \boldsymbol{\Sigma}) \triangleq \frac{1}{\pi^N \det(\boldsymbol{\Sigma})} \mathrm{e}^{-(\mathbf{x}-\boldsymbol{\mu})^{\mathsf{H}} \boldsymbol{\Sigma}^{-1} (\mathbf{x}-\boldsymbol{\mu})}$. $\mathcal{U}[a, b)$ denotes the uniform distribution in $[a, b)$.

Expectation of function $\mathsf{g}(\cdot)$ of random variable x with probability density function (PDF) $\mathsf{f}_x(\cdot)$ is denoted as $\mathbb{E}[\mathsf{g}(x)] \triangleq \int_x \mathsf{g}(x) \mathsf{f}_x(x) \mathsf{d}x$. The probability of event $\mathcal{A}$ is denoted as $\mathbb{P}(\mathcal{A})$.

II. System Model

A. Network Architecture

A scatter radio WSN consists of N static sensors (tags) at distinct positions that backscatter their measured data to a

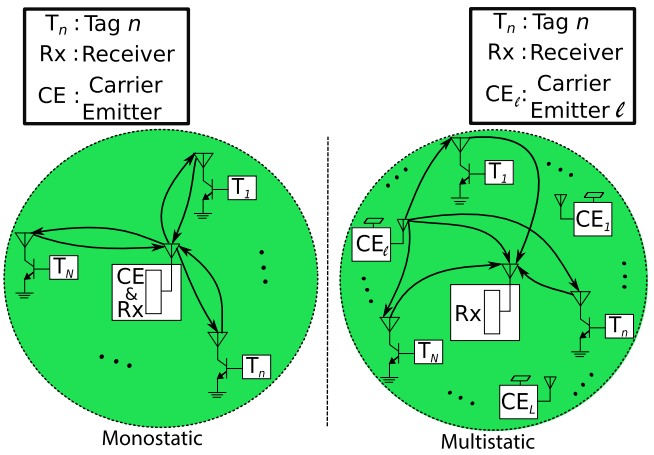

Fig. 1. Monostatic (Left) and Multistatic (Right) WSN architecture with N tags, $n = 1 \dots N$, and L illuminating carrier emitters (CEs), $l = 1 \dots L$.

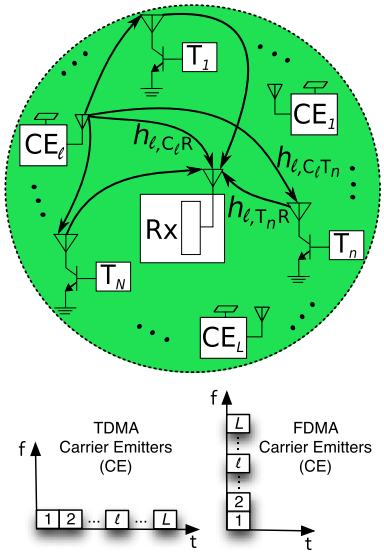

Fig. 2. Multi-user multistatic transmission model over the l-th time slot.

single software-defined radio (SDR) reader; the set of tags is denoted as $\mathcal{N} \triangleq \{1, 2, \dots, N\}$. Tags/sensors are considered *semi-passive*, i.e., they utilize scatter radio for communication and obtain required power for operation from any type of energy source, either ambient (solar, thermoelectric, chemical) or dedicated (e.g., battery). However, Section VI will contrast monostatic and multistatic architectures for *passive* tags as well, which solely harvest energy from the illuminator(s).

The multistatic network architecture assumes a set of carrier emitters (CE), denoted as $\mathcal{L} \triangleq \{1, 2, \dots, L\}$. The CEs are distinct units from the SDR receiver and transmit a continuous carrier wave (CW) with time-division multiple access (TDMA) or frequency-division multiple access (FDMA) (Fig. 1-Right and Fig. 2). In CEs with TDMA, the l-th CE transmits at the l-th *time* slot using a common carrier frequency. In CE FDMA, the l-th CE transmits at the l-th *frequency* slot, i.e., carrier frequency centered at a frequency band orthogonal to the bands of the other simultaneously (in-time) transmitting CEs. The wireless channel is assumed quasi-static, changing independently across different (time or frequency) slots. For the l-th (time or frequency) slot, there are $2N+1$ unidirectional links (N CE-to-tag links, N tag-to-SDR reader links and the CE-to-SDR reader link). The distance between the l-th CE and the n-th tag is denoted by $\mathsf{d}_{\mathrm{C}_l\mathrm{T}_n}$, the distance between the n-th tag and the reader is denoted as $\mathsf{d}_{\mathrm{T}_n\mathrm{R}}$ with $n \in \mathcal{N}$ and the distance between the l-th CE and the SDR reader is denoted as $\mathsf{d}_{\mathrm{C}_l\mathrm{R}}$ (Fig. 2). We will show that TDMA and FDMA for CEs offer equivalent signal representations under the assumptions of this work.

The monostatic architecture assumes that the single-antenna reader functions as both the receiver and the CW emitter, in full-duplex mode. Specifically, the reader transmits the illuminating carrier towards the tags, which in turn modulate their information on the reflected (and scattered back) signal towards the SDR reader. For fair comparison to the multistatic case, transmission across L time slots will be also assumed, with wireless channel changing independently between time slots. In this architecture N bidirectional links exist, i.e., between the reader and the N tags (Fig. 1-Left). The distance between the reader and the n-th tag is denoted by d_{k}, where $\mathrm{k} \in \{\mathrm{T}_n\mathrm{R}, \mathrm{RT}_n\}$ denotes the unidirectional tag-to-reader, reader-to-tag link, respectively.

Let $\mathbf{u}_{\mathrm{T}_n}$, $n \in \mathcal{N}$, $\mathbf{u}_{\mathrm{C}_l}$, $l \in \mathcal{L}$, and $\mathbf{u}_{\mathrm{R}}$ denote the position of n-th tag, l-th CE, and SDR reader, respectively.

B. Channel Model

The following path-loss model is adopted [29]:

$$\mathsf{L}_{\mathrm{k}} = \left(\frac{\lambda}{4\pi d_0}\right)^2 \left(\frac{d_0}{\mathsf{d}_{\mathrm{k}}}\right)^{\nu_{\mathrm{k}}}, \tag{1}$$

where $\mathrm{k} \in \{\mathrm{C}_l\mathrm{R}, \mathrm{C}_l\mathrm{T}_n, \mathrm{T}_n\mathrm{R}\}$ for multistatic and $\mathrm{k} \in \{\mathrm{T}_n\mathrm{R}, \mathrm{RT}_n\}$ for monostatic architecture, d_0 is a reference distance (assumed unit thereinafter), λ is the carrier emission wavelength and ν_{k} is the path-loss exponent for link k.

Tag communication bandwidth and channel delay spread are assumed relatively small and thus, frequency non-selective (flat) fading is assumed: complex channel gain for the l-th (time or frequency) slot is denoted as $h_{l,\mathrm{k}} = a_{l,\mathrm{k}}\, \mathsf{e}^{-\mathrm{j}\phi_{l,\mathrm{k}}}$, where $a_{l,\mathrm{k}} \in \mathbb{R}_+$, $\phi_{l,\mathrm{k}} \in [0, 2\pi)$, $\mathrm{k} \in \{\mathrm{C}_l\mathrm{R}, \mathrm{C}_l\mathrm{T}_n, \mathrm{T}_n\mathrm{R}\}$ and $\mathrm{k} \in \{\mathrm{T}_n\mathrm{R}, \mathrm{RT}_n\}$ for multistatic and monostatic architecture, respectively, with $\mathbb{E}\left[|h_{l,\mathrm{k}}|^2\right] \equiv \mathbb{E}\left[a_{l,\mathrm{k}}^2\right] = 1$. It is emphasized that for CEs in TDMA or FDMA mode, $h_{l_1,\mathrm{k}}$ is statistically independent to $h_{l_2,\mathrm{k}}$ for any $l_1 \neq l_2$. Moreover, at the monostatic architecture reciprocity implies $h_{l,\mathrm{T}_n\mathrm{R}} = h_{l,\mathrm{RT}_n}$, while at the multistatic architecture, $\{h_{l,\mathrm{k}}\}$ are independent (and not necessarily identically distributed) for different $\mathrm{k} \in \{\mathrm{C}_l\mathrm{R}, \mathrm{C}_l\mathrm{T}_n, \mathrm{T}_n\mathrm{R}\}$.[1]

Due to potentially strong line-of-sight (LoS) signals in scatter radio environments, Nakagami small-scale fading is assumed (with $\mathbb{E}\left[a_{l,\mathrm{k}}^2\right] = 1$) [29, p. 79]:

$$\mathsf{f}_{a_{l,\mathrm{k}}}(x) = 2\,(\mathtt{M}_{\mathrm{k}})^{\mathtt{M}_{\mathrm{k}}} \frac{x^{2\mathtt{M}_{\mathrm{k}}-1}}{\Gamma(\mathtt{M}_{\mathrm{k}})}\, \mathsf{e}^{-\mathtt{M}_{\mathrm{k}}x^2}, \quad x \geq 0, \tag{2}$$

[1]Results can be easily extended to the multi-antenna reader case.

where $\mathtt{M}_\mathrm{k} \geq \frac{1}{2}$ is the Nakagami parameter and function $\Gamma(x) = \int_0^\infty t^{x-1}\mathrm{e}^{-t}\mathrm{d}t$ is the Gamma function. For the special cases of $\mathtt{M}_\mathrm{k} = 1$ and $\mathtt{M}_\mathrm{k} = \infty$, Rayleigh (i.e., NLoS scenarios) and zero fading (i.e., $a_{l,\mathrm{k}} = 1$) is obtained, respectively. For $\mathtt{M}_\mathrm{k} = \frac{(\kappa_\mathrm{k}+1)^2}{2\kappa_\mathrm{k}+1}$, the distribution in (2) approximates Rice with Rician parameter κ_k, where commonly $\kappa_\mathrm{k} \in [0, 20]$ [29].[2] It is noted that the adopted small-scale fading model can accommodate either LoS or NLoS scenarios by alternating the value of Nakagami parameter $\mathtt{M}$ for each scatter radio link.

C. Signal Model

1) Multistatic: The l-th CE transmits a CW at the l-th (time or frequency) slot, with complex baseband $q_l^{[\mathrm{b}]}(t) = \sqrt{2\,P_{\mathrm{C}_l}}\,\mathrm{e}^{-\mathrm{j}(2\pi\Delta F_l t + \Delta\phi_l)}$, where P_{C_l} is the l-th CE transmission power, while ΔF_l and $\Delta\phi_l$ model the carrier frequency offset (CFO) and phase offset between the l-th CE and the SDR reader, respectively, due to the fact that CE and the SDR reader do not share the same oscillator.

Each tag $n \in \mathcal{N}$ is illuminated by the carrier wave $q_l^{[\mathrm{b}]}(t)$. The tag's information is binary-modulated on the incident CW by switching the antenna load between two loads, associated with two distinct reflection coefficients: $\Gamma_{n,0}$ and $\Gamma_{n,1}$ for bit "0" and bit "1", respectively. For scatter radio, binary frequency-shift keying (FSK) is assumed in this work, where each tag switches between the two loads using a 50% duty cycle square waveform of duration T per bit (nominal bit duration), fundamental frequency $F_{n,i}$, and random initial phase $\Phi_{n,i}$, for bit $i \in \mathbb{B} \triangleq \{0, 1\}$; in other words, modulation occurs with different switching frequency between tag antenna loads, utilizing switching (also coined as *subcarrier*) frequency $F_{n,0}$ for bit "0" and $F_{n,1}$ for bit "1", without any type of signal conditioning, such as filtering, amplification or mixing [1].

Fig. 3 shows the measured spectrum at a spectrum analyzer when a signal's generator's CW at $F_s = 868$ MHz illuminates tag n that utilizes binary FSK with $|F_{n,1} - F_{n,0}| = 122.5$ kHz. In contrast to classic (Marconi-radio) FSK, frequencies $F_s - F_{n,0}$ and $F_s - F_{n,1}$ also contribute to the total signal (in addition to $F_s + F_{n,0}$ and $F_s + F_{n,1}$) [1] and thus, backscatter FSK modulation uses 4 frequencies, $\pm F_{n,i_n}$, $i_n \in \mathbb{B}$. Therefore, the optimal receiver requires 4 matched filters and not 2, as in classic FSK demodulation.

Each tag n can use a *unique* set of subcarrier frequencies $F_{n,i_n}, i_n \in \mathbb{B}$ to scatter its information. At the network level, the $4N$ frequencies $\{\pm F_{n,i_n}\}, \forall (i_n, n) \in \mathbb{B} \times \mathcal{N}$ must satisfy the orthogonality criterion, which for coherent FSK adheres to the following[3]:

$$|F_{n,i} - F_{j,m}| = \frac{k}{2T} \quad \text{and} \quad F_{n,i} \gg \frac{1}{2T}, \tag{3}$$

$\forall (i, n),\ (m, j) \in \mathbb{B} \times \mathcal{N} : m \neq i$, and $k \in \mathbb{N}$.

This implies that the system of N tags scattering simultaneously can be divided into N parallel orthogonal channels,

[2]For the calculation of bit error rate under noncoherent detection, phases $\phi_{l,\mathrm{k}}$ are assumed uniformly distributed over $[0, 2\pi)$. The expressions for the rest metrics are independent of the distribution of phases $\phi_{l,\mathrm{k}}$.

[3]For noncoherent FSK, term $k/2T$ in Eq. (3) is replaced with k/T.

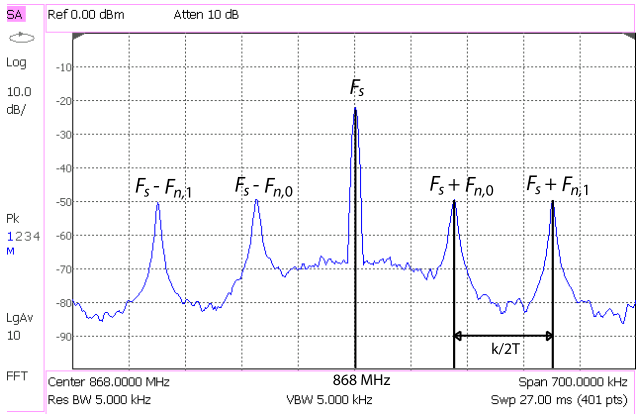

Fig. 3. Measured backscatter radio FSK spectrum with two loads. Scattered signal appears in 4 frequencies, 2 left and 2 right of the illuminating carrier.

where each can be received separately, without collision. Such single-tag processing techniques have been extensively covered in [1], [16], [18], and [19]. At the l-th slot, the CFO-free, DC-blocked received baseband signal at the reader over a bit period T from tag n, excluding higher harmonics, is given by [19, eq. (13)] and [18, eq. (12)]:

$$\mathbf{r}_{l,n}^{[\mathrm{b}]} = h_{l,n}^{[\mathrm{b}]}\sqrt{\mathtt{E}_{l,n}^{[\mathrm{b}]}}\,\mathbf{x}_n + \mathbf{w}_{l,n}, \quad n \in \mathcal{N}, \tag{4}$$

where the vector $\mathbf{x}_n$ is defined as:

$$\mathbf{x}_n \triangleq \sqrt{\frac{1}{2}}\left[\mathrm{e}^{+\mathrm{j}\Phi_{n,0}}\ \mathrm{e}^{-\mathrm{j}\Phi_{n,0}}\ \mathrm{e}^{+\mathrm{j}\Phi_{n,1}}\ \mathrm{e}^{-\mathrm{j}\Phi_{n,1}}\ \right]^\top \odot \mathbf{v}_{i_n}, \tag{5}$$

$n \in \mathcal{N}$, where $\mathbf{v}_{i_n} = [(1-i_n)\ \ (1-i_n)\ \ i_n\ \ i_n]^\top$ is the four-dimensional transmitted symbol of the n-th tag corresponding to transmitted bit $i_n \in \mathbb{B}$. $\Phi_{n,0}$ ($\Phi_{n,1}$) is implementation-specific phase mismatch between tag n and reader for bit 0 (bit 1), assumed constant for the L slots. Symbol $\odot$ denotes the component-wise (Hadamard) product. For $F_{n,i_n} + \frac{20}{T} \ll W_{\mathrm{SDR}}$, where W_{SDR} is the SDR receiver baseband bandwidth, $\mathbf{w}_{l,n} \sim \mathcal{CN}(\mathbf{0}_4, N_0\,\mathbf{I}_4)$ [19, Th. 1], with $N_0 = \mathrm{k_b T}_\theta/2$, where $\mathrm{k_b}$ and T_θ are the Boltzmann constant and receiver temperature, respectively. $h_{l,n}^{[\mathrm{b}]}$ in Eq. (4) is given by:

$$h_{l,n}^{[\mathrm{b}]} \triangleq a_{l,n}^{[\mathrm{b}]}\,\mathrm{e}^{-\mathrm{j}\phi_{l,n}^{[\mathrm{b}]}}, \tag{6}$$

$$a_{l,n}^{[\mathrm{b}]} = a_{l,\mathrm{C}_l\mathrm{T}_n}\,a_{l,\mathrm{T}_n\mathrm{R}}, \tag{7}$$

$$\phi_{l,n}^{[\mathrm{b}]} = \phi_{l,\mathrm{C}_l\mathrm{T}_n} + \phi_{l,\mathrm{T}_n\mathrm{R}} + \Delta\phi_l + \underline{\angle\Gamma_{n,0} - \Gamma_{n,1}}. \tag{8}$$

Symbol $\mathtt{E}_{l,n}^{[\mathrm{b}]}$ denotes the average energy per bit for the n-th tag over the l-th slot given by [18, eq. (9)]:

$$\mathtt{E}_{l,n}^{[\mathrm{b}]} = \frac{\mathbb{E}\left[\left(a_{l,n}^{[\mathrm{b}]}\,\mu_{l,n}^{[\mathrm{b}]}\right)^2 T\right]}{2} = \frac{\left(\mu_{l,n}^{[\mathrm{b}]}\right)^2 T}{2}, \tag{9}$$

taking into account that RVs $a_{l,\mathrm{C}_l\mathrm{T}_n}$ and $a_{l,\mathrm{T}_n\mathrm{R}}$ are independent with unit average squared value. The following is also employed:

$$\mu_{l,n}^{[\mathrm{b}]} = \sqrt{2\,P_{\mathrm{C}_l}\,\mathtt{L}_{\mathrm{C}_l\mathrm{T}_n}\,\mathtt{L}_{\mathrm{T}_n\mathrm{R}}}\,|\Gamma_{n,0} - \Gamma_{n,1}|\,\frac{2}{\pi}\,\mathtt{s}_n, \tag{10}$$

with $\mathtt{s}_n$ modeling the n-th tag's (real) scattering efficiency, assumed constant. The average received SNR of tag n at the

l-th slot for multistatic system associated with the system in Eq. (4) is given by $\mathtt{SNR}_{l,n}^{[\mathrm{b}]} = \mathtt{E}_{l,n}^{[\mathrm{b}]}/N_0$.

As already mentioned, for CEs in TDMA or FDMA mode, $h_{l_1,\mathrm{k}}$ is statistically independent to $h_{l_2,\mathrm{k}}$ for any $l_1 \neq l_2$. Under this assumption, tools developed in this work can in principle accommodate both CE modes. For simpler presentation and concise comparison with the monostatic architecture, we will assume hereinafter CEs in TDMA mode.

2) Monostatic: Due to the fact that the receiver and the emitter share the same oscillator, CFO ΔF_l and phase offset $\Delta\phi_l$ are zero in the monostatic case. Using Eq. (4) and the reciprocity of the channel between the reader and each tag, the DC-blocked, demodulated received signal for tag n in the monostatic architecture at time slot l is given by:

$$\mathbf{r}_{l,n}^{[\mathrm{m}]} = h_{l,n}^{[\mathrm{m}]} \sqrt{\frac{\mathtt{M}_n}{\mathtt{M}_n+1}\mathtt{E}_n^{[\mathrm{m}]}}\,\mathbf{x}_n + \mathbf{w}_{l,n}, \quad n \in \mathcal{N}, \tag{11}$$

under the same assumptions and definitions as in Eqs. (4), (5). In accordance with the multistatic case, $h_{l,n}^{[\mathrm{m}]}$ is given by:

$$h_{l,n}^{[\mathrm{m}]} \triangleq a_{l,n}^{[\mathrm{m}]}\, \mathtt{e}^{-\mathrm{j}\phi_{l,n}^{[\mathrm{m}]}}, \tag{12}$$

$$a_{l,n}^{[\mathrm{m}]} = \left(a_{l,\mathrm{T}_n\mathrm{R}}\right)^2,\ \phi_{l,n}^{[\mathrm{m}]} = 2\phi_{l,\mathrm{T}_n\mathrm{R}} + \underline{\Gamma_{n,0} - \Gamma_{n,1}}. \tag{13}$$

The average received energy per bit for monostatic system for the n-th tag over the l-th time slot, $\mathtt{E}_n^{[\mathrm{m}]}$, is expressed as:

$$\mathtt{E}_n^{[\mathrm{m}]} = \frac{\mathbb{E}\left[\left(a_{l,n}^{[\mathrm{m}]}\,\mu_{l,n}^{[\mathrm{m}]}\right)^2 T\right]}{2} = \frac{1+\mathtt{M}_n}{2\,\mathtt{M}_n}\left(\mu_n^{[\mathrm{m}]}\right)^2 T, \tag{14}$$

since $\mathbb{E}\left[\left(a_{l,n}^{[\mathrm{m}]}\right)^2\right] = \mathbb{E}\left[\left(a_{l,\mathrm{T}_n\mathrm{R}}\right)^4\right] = (\mathtt{M}_n+1)/\mathtt{M}_n$ and $\mu_n^{[\mathrm{m}]}$ is simplified from Eq. (10) to:

$$\mu_n^{[\mathrm{m}]} = \sqrt{2\,P_{\mathrm{R}}}\,\mathtt{L}_{\mathrm{T}_n\mathrm{R}}\,|\Gamma_{n,0} - \Gamma_{n,1}|\,\frac{2}{\pi}\,\mathtt{s}_n. \tag{15}$$

The average received SNR of tag n at the l-th time slot for monostatic system is given by[4] $\mathtt{SNR}_n^{[\mathrm{m}]} = \mathtt{E}_n^{[\mathrm{m}]}/N_0$.

It is emphasized that the quantities $\mathtt{E}_n^{[\mathrm{m}]}$ and $\mathtt{SNR}_n^{[\mathrm{m}]}$ in the monostatic case above, do not depend on time index l, because they are functions of path-loss $\mathtt{L}_{\mathrm{T}_n\mathrm{R}}$; the latter remains unaffected during the L slots. In contrast, $\mathtt{E}_{l,n}^{[\mathrm{b}]}$ and $\mathtt{SNR}_{l,n}^{[\mathrm{b}]}$ in the multistatic case, are both functions of path-loss $\mathtt{L}_{\mathrm{C}_l\mathrm{T}_n}$, which depends on the slot index l, since different CE corresponds to each slot.

In addition, it is noted that due to the nature of FSK modulation, the discrete baseband signal expressions in Eqs. (4) and (11) depend solely on links $\mathrm{C}_l\mathrm{T}_n$ and $\mathrm{T}_n\mathrm{R}$ due to DC-blocking operation, and thus, the analysis is continued with link $\mathrm{T}_n\mathrm{R}$ for monostatic and links $\mathrm{C}_l\mathrm{T}_n$ and $\mathrm{T}_n\mathrm{R}$ for bistatic (one CE) or multistatic (multiple CEs) architecture, $\forall (l,n) \in \mathcal{L}\times\mathcal{N}$.

III. BER Analysis With ML Detection

A. Distribution of Fading Amplitudes

It can be observed that RVs $(a_{l,\mathrm{C}_l\mathrm{T}_n})^2$ and $(a_{l,\mathrm{T}_n\mathrm{R}})^2$ are independent following Gamma distribution with parameters $\left(\mathtt{M}_{\mathrm{C}_l\mathrm{T}_n}, \frac{1}{\mathtt{M}_{\mathrm{C}_l\mathrm{T}_n}}\right)$ and $\left(\mathtt{M}_{\mathrm{T}_n\mathrm{R}}, \frac{1}{\mathtt{M}_{\mathrm{T}_n\mathrm{R}}}\right)$, respectively [30, p. 242], i.e., the probability density function (PDF) of RV $(a_{l,\mathrm{k}})^2$ is given by:

$$\mathtt{f}_{a_{l,\mathrm{k}}^2}(x) = (\mathtt{M}_{\mathrm{k}})^{\mathtt{M}_{\mathrm{k}}}\,\frac{x^{\mathtt{M}_{\mathrm{k}}-1}}{\Gamma(\mathtt{M}_{\mathrm{k}})}\,\mathtt{e}^{-\mathtt{M}_{\mathrm{k}}x}, \quad x \geq 0, \tag{16}$$

$\mathrm{k} \in \{\mathrm{C}_l\mathrm{T}_n, \mathrm{T}_n\mathrm{R}\}$. The above distribution reflects the power distribution of each small-scale fading scatter radio link for both monostatic and multistatic architectures and will be used as a building block to derive closed-form expressions for the metrics of interest.

For simplified notation, the following abbreviations are used: $\mathtt{M}_{\mathrm{C}_l\mathrm{T}_n} = \mathtt{M}_{ln}$ and $\mathtt{M}_{\mathrm{T}_n\mathrm{R}} = \mathtt{M}_n$.

B. Coherent

1) Monostatic: According to Eq. (11), the conditional bit error rate (BER) for tag n over time slot l, given channel realization $h_{l,n}^{[\mathrm{m}]}$ (with $\left|h_{l,n}^{[\mathrm{m}]}\right| = a_{l,n}^{[\mathrm{m}]}$) and phase parameters $\Phi_{n,0}, \Phi_{n,1}$ under ML coherent detection depends solely on amplitude $a_{l,n}^{[\mathrm{m}]}$ [19], and is given by [31, p. 508]:

$$\begin{aligned}\mathbb{P}\left(e_{l,n}^{[\mathrm{m}]} \mid a_{l,n}^{[\mathrm{m}]}\right) &= \mathtt{Q}\left(\frac{a_{l,n}^{[\mathrm{m}]}\sqrt{\frac{\mathtt{M}_n}{\mathtt{M}_n+1}\mathtt{E}_n^{[\mathrm{m}]}}\,\left\|\mathbf{x}_0-\mathbf{x}_1\right\|_2}{\sqrt{2\,N_0}}\right)\\ &= \mathtt{Q}\left(a_{l,n}^{[\mathrm{m}]}\sqrt{\frac{\mathtt{M}_n\mathtt{SNR}_n^{[\mathrm{m}]}}{\mathtt{M}_n+1}}\right),\end{aligned} \tag{17}$$

where function $\mathtt{Q}(x) = \frac{1}{2\pi}\int_x^\infty \mathtt{e}^{-\frac{t^2}{2}}\mathtt{d}t$ and $\left\|\mathbf{x}_0-\mathbf{x}_1\right\|_2 = \sqrt{2}$ were utilized.

Using the Chernoff bound for $\mathtt{Q}(\cdot)$ function, Eq. (17) can be upper bounded as $\mathtt{Q}\left(a_{l,n}^{[\mathrm{m}]}\sqrt{\frac{\mathtt{M}_n\mathtt{SNR}_n^{[\mathrm{m}]}}{\mathtt{M}_n+1}}\right) \leq \frac{1}{2}\,\mathtt{e}^{-\frac{\left(a_{l,n}^{[\mathrm{m}]}\right)^2\mathtt{M}_n\,\mathtt{SNR}_n^{[\mathrm{m}]}}{2\,(\mathtt{M}_n+1)}}$. Since RV $a_{l,n}^{[\mathrm{m}]} = (a_{l,\mathrm{T}_n\mathrm{R}})^2$ follows Gamma distribution with parameter $\left(\mathtt{M}_n, \frac{1}{\mathtt{M}_n}\right)$, the unconditional BER can be bounded as follows:

$$\begin{aligned}\mathbb{P}\left(e_{l,n}^{[\mathrm{m}]}\right) &= \mathop{\mathbb{E}}_{a_{l,n}^{[\mathrm{m}]}}\left[\mathbb{P}\left(e_{l,n}^{[\mathrm{m}]} \mid a_{l,n}^{[\mathrm{m}]}\right)\right]\\ &\overset{(a)}{\leq} \int_0^\infty \frac{1}{2}\,\mathtt{e}^{-\frac{x^2\,\mathtt{M}_n\,\mathtt{SNR}_n^{[\mathrm{m}]}}{2\,(\mathtt{M}_n+1)}}\,(\mathtt{M}_n)^{\mathtt{M}_n}\,\frac{x^{\mathtt{M}_n-1}}{\Gamma(\mathtt{M}_n)}\,\mathtt{e}^{-\mathtt{M}_n x}\mathtt{d}x\\ &\overset{(b)}{=} \frac{1}{2}\left(\frac{\mathtt{M}_n+\mathtt{M}_n^2}{2\,\mathtt{SNR}_n^{[\mathrm{m}]}}\right)^{\frac{\mathtt{M}_n}{2}}\mathtt{U}\left(\frac{\mathtt{M}_n}{2}, \frac{1}{2}, \frac{\mathtt{M}_n+\mathtt{M}_n^2}{2\,\mathtt{SNR}_n^{[\mathrm{m}]}}\right),\end{aligned} \tag{18}$$

where $\mathtt{U}(\cdot,\cdot,\cdot)$ is the confluent hypergeometric function [32, eq. (13.4.4)]. In step (a) above, the Chernoff bound for Q function was exploited and in step (b), [33, eq. (3.462.1) and eq. (9.240)] and then [32, eq. (13.14.3)] were utilized to simplify the final formula.

Is is emphasized that BER of Eq. (18) depends on $\mathtt{SNR}_n^{[\mathrm{m}]}$ of tag n, which in turn, depends on Eq. (14); the latter is a function of tag's n location through Eq. (15). Thus, the above BER expression depends on the topology of the tags. The following proposition offers an important, topology-independent metric:

[4]From Eq. (11), notice that $\mathbb{E}\left[|h_{l,n}^{[\mathrm{m}]}|^2\,\frac{\mathtt{M}_n}{\mathtt{M}_n+1}\mathtt{E}_n^{[\mathrm{m}]}||\mathbf{x}_n||^2\right] = \mathtt{E}_n^{[\mathrm{m}]}$.

Proposition 1: Under Rayleigh fading, i.e., $\mathtt{M}_n = 1$, monostatic architecture offers diversity order equal to $1/2$ for any $(l,n) \in \mathcal{L} \times \mathcal{N}$.

Proof: The proof is given in Appendix A. ∎

The above result indicates that for any slot under Rayleigh fading, monostatic BER decays inversely proportional with square root of SNR at the high SNR regime. It is shown below that the decay is faster in the multistatic case.

2) Multistatic: Exploiting Eq. (7) along with the formula in [30, p. 302. eq. (6.148)], the PDF of the product $g_{l,n}^{[\mathrm{b}]} \triangleq \left(a_{l,n}^{[\mathrm{b}]}\right)^2 = (a_{l,\mathrm{C}_l\mathrm{T}_n})^2\,(a_{l,\mathrm{T}_n\mathrm{R}})^2$ can be expressed in closed form as follows ($x \geq 0$):

$$\begin{aligned}\mathsf{f}_{g_{l,n}^{[\mathrm{b}]}}(x) &= \int_0^\infty \frac{1}{y}\,\mathsf{f}_{a^2_{l,\mathrm{C}_l\mathrm{T}_n}}(y)\,\mathsf{f}_{a^2_{l,\mathrm{T}_n\mathrm{R}}}\left(\frac{x}{y}\right)\mathsf{d}y \\ &= \frac{2(x\,\mathtt{M}_{ln}\,\mathtt{M}_n)^{\frac{\mathtt{M}_{ln}+\mathtt{M}_n}{2}}\,\mathsf{K}_{\mathtt{M}_n-\mathtt{M}_{ln}}\left(2\sqrt{\mathtt{M}_{ln}\,\mathtt{M}_n\,x}\right)}{x\,\Gamma(\mathtt{M}_{ln})\,\Gamma(\mathtt{M}_n)}, \quad (19)\end{aligned}$$

where [33, eq. (3.471.9)] was used to obtain the simplified form in Eq. (19). $\mathsf{K}_\nu(\cdot)$ is the ν-th order modified Bessel function of the second kind, satisfying $\mathsf{K}_\nu(\cdot) = \mathsf{K}_{-\nu}(\cdot)$ [32, eq. (10.27.3)]. The above distribution is the power distribution of Nakagami dyadic backscatter channel. Similar expression with Eq. (19) can be found in [34], while a derivation of Eq. (19) in the special case of $\mathtt{M}_{ln} = \mathtt{M}_n$ is given in [35].

In the multistatic case, according to Eq. (4), the conditional BER for tag n over the l-th time slot is given by:

$$\mathbb{P}\left(e_{l,n}^{[\mathrm{b}]} \mid a_{l,n}^{[\mathrm{b}]}\right) = \mathsf{Q}\left(a_{l,n}^{[\mathrm{b}]}\sqrt{\mathtt{SNR}_{l,n}^{[\mathrm{b}]}}\right), \quad (20)$$

which with the use of Chernoff bound is upper bounded as $\mathsf{Q}\left(a_{l,n}^{[\mathrm{b}]}\sqrt{\mathtt{SNR}_{l,n}^{[\mathrm{b}]}}\right) \leq \frac{1}{2}\,\mathsf{e}^{-\frac{\left(a_{l,n}^{[\mathrm{b}]}\right)^2\,\mathtt{SNR}_{l,n}^{[\mathrm{b}]}}{2}}$.

Hence, the BER over the l-th slot for the n-th tag is upper bounded as follows:

$$\begin{aligned}\mathbb{P}\left(e_{l,n}^{[\mathrm{b}]}\right) &= \mathop{\mathbb{E}}_{a_{l,n}^{[\mathrm{b}]}}\left[\mathbb{P}\left(e_{l,n}^{[\mathrm{b}]}|a_{l,n}^{[\mathrm{b}]}\right)\right] \leq \int_0^\infty \mathsf{e}^{\left(-x\mathtt{SNR}_{l,n}^{[\mathrm{b}]}/2\right)} \\ &\quad\times \frac{(x\,\mathtt{M}_{ln}\,\mathtt{M}_n)^{\frac{\mathtt{M}_{ln}+\mathtt{M}_n}{2}}\,\mathsf{K}_{\mathtt{M}_n-\mathtt{M}_{ln}}\left(2\sqrt{\mathtt{M}_{ln}\,\mathtt{M}_n\,x}\right)}{x\,\Gamma(\mathtt{M}_{ln})\,\Gamma(\mathtt{M}_n)}\mathsf{d}x \\ &\overset{(a)}{=} \frac{1}{2}\left(\frac{2\,\mathtt{M}_{ln}\mathtt{M}_n}{\mathtt{SNR}_{l,n}^{[\mathrm{b}]}}\right)^{\mathtt{M}_n}\mathsf{U}\left(\mathtt{M}_n, 1+\mathtt{M}_n-\mathtt{M}_{ln}, \frac{2\,\mathtt{M}_{ln}\mathtt{M}_n}{\mathtt{SNR}_{l,n}^{[\mathrm{b}]}}\right), \quad (21)\end{aligned}$$

where $\mathsf{U}(\cdot,\cdot,\cdot)$ is the confluent hypergeometric function [32, eq. (13.4.4)]. In Step (a) above, change of variables $x = y^2$ is applied and then [33, eq. (6.631.3)] and [32, eq. (13.14.3)] are exploited to simplify the final expression.

BER of Eq. (21) also depends on the network topology, through the definition of $\mathtt{SNR}_{l,n}^{[\mathrm{b}]}$ and energy per bit per slot in Eqs. (9) and (10). The following proposition offers a topology-independent metric:

Proposition 2: Under Rayleigh fading, i.e., $\mathtt{M}_{ln} = \mathtt{M}_n = 1$, multistatic architecture offers diversity order *at least* 1 for any $(l,n) \in \mathcal{L} \times \mathcal{N}$.

Proof: The proof is given in Appendix B. ∎

Thus, it is concluded that under Rayleigh fading, the multistatic BER drops faster compared to the monostatic, at the high SNR regime, even for a single, fixed slot.

C. Noncoherent

To better highlight the importance of the expressions derived in Eqs. (18) and (21), consider the n-th tag operating in noncoherent reception mode over the l-th slot. For fixed dyadic backscatter channel amplitudes $a_{l,n}^{[\mathrm{m}]}$ and $a_{l,n}^{[\mathrm{b}]}$, as well as phase offsets $\Phi_{n,0}$ and $\Phi_{n,1}$, and unknown dyadic backscatter channel angles $\phi_{l,n}^{[\mathrm{m}]}$ and $\phi_{l,n}^{[\mathrm{b}]}$, it is not difficult to show that the ML reception rule for orthogonal signaling is based on envelope detection [36, Eq. (4.5-32)] of the 4×1 complex received vector $\mathbf{r}_{l,n}$ and takes the following form:

$$\left|\mathbf{r}_{l,n}^{[\mathrm{x}]}[1] + \mathsf{e}^{2\mathrm{j}\Phi_{n,0}}\mathbf{r}_{l,n}^{[\mathrm{x}]}[2]\right| \underset{i_n=1}{\overset{i_n=0}{\gtrless}} \left|\mathbf{r}_{l,n}^{[\mathrm{x}]}[3] + \mathsf{e}^{2\mathrm{j}\Phi_{n,1}}\mathbf{r}_{l,n}^{[\mathrm{x}]}[4]\right|, \quad (22)$$

where $\mathrm{x} = \mathrm{m}$, $\mathrm{x} = \mathrm{b}$, for monostatic and multistatic system, respectively. Note that the above rule requires the received signal vector $\mathbf{r}_{l,n}^{[\mathrm{x}]}$ and the tag n implementation-specific phases $\Phi_{n,0}$ and $\Phi_{n,1}$, while it is different than the square-law detector: $|\mathbf{r}_{l,n}[1]|^2 + |\mathbf{r}_{l,n}[2]|^2 \underset{i_n=1}{\overset{i_n=0}{\gtrless}} |\mathbf{r}_{l,n}[3]|^2 + |\mathbf{r}_{l,n}[4]|^2$ in [16]. Following the same lines in [36, pp. 217–218], the corresponding conditional error probability of rule in Eq. (22) is $\frac{1}{2}\,\mathsf{e}^{-\frac{\left(a_{l,n}^{[\mathrm{m}]}\right)^2\,\mathtt{M}_n\,\mathtt{SNR}_n^{[\mathrm{m}]}}{2\,(\mathtt{M}_n+1)}}$ and $\frac{1}{2}\,\mathsf{e}^{-\frac{\left(a_{l,n}^{[\mathrm{b}]}\right)^2\mathtt{SNR}_n^{[\mathrm{b}]}}{2}}$ for monostatic and multistatic systems, respectively. Note that the above expressions coincide with the upper bounds of conditional error probabilities given in Eq. (17) and (20). In other words, the expressions in (18) and (21) reflect the exact BER performance under noncoherent envelope detection in monostatic and multistatic architecture, respectively.[5]

IV. Information Outage Analysis

Section II assumed that all switching (subcarrier) frequencies used by the tags adhere to the orthogonality criterion given in Eq. (3). In practice, that may not be always feasible due to frequency generation constraints (e.g., clock drifts, lack of phase-locked loops). As a result, tags may be allocated to distinct subcarrier frequencies, which may cause adjacent channel interference. Due to the roundtrip nature of signal propagation in scatter radio (i.e., from illuminator to tag and back to reader), an adjacent in frequency tag j, i.e., tag with pair of subcarrier frequencies $(F_{j,0}, F_{j,1})$ relatively *close* to $(F_{n,0}, F_{n,1})$, may be received with significantly higher power than the tag of interest n; thus, any deviation from the orthogonality criterion may cause interference. Therefore, the relative spatial location of one tag versus the other, i.e., network topology, as well as the subcarrier frequency allocation (denoted as $\mathcal{C}$) of N available pairs of subcarrier frequencies to N tags does affect overall performance in practice. Notice that there are $N!$ possible subcarrier frequency assignments to N tags. In this section, set $\mathcal{A}(n) \triangleq \mathcal{N}\backslash n$ denotes the tags

[5]Results are connected with the signal model of Section II, which assumes perfect CFO estimation and correction (in the multistatic case) and perfect DC blocking at the baseband signal for both monostatic and multistatic cases.

that interfere the reception of tag n, $g_{l,n}^{[\mathrm{m}]} = \left(a_{l,n}^{[\mathrm{m}]}\right)^2$ and $g_{l,n}^{[\mathrm{b}]} = \left(a_{l,n}^{[\mathrm{b}]}\right)^2$. For simplification in the followed analysis, it is also assumed that $g_{l,n}$ and $g_{l,j}$ are statistically independent among different tags $(n \neq j)$, for any $l \in \mathcal{L}$.

A. Monostatic

For a given subcarrier frequency assignment $\mathcal{C}$, incorporating imperfections as mentioned above, the *instantaneous* signal-to-interference-plus-noise ratio (SINR) of tag n at the l-th time slot is given by:

$$\mathrm{SINR}_{l,n}^{[\mathrm{m}]}(\mathcal{C}) \triangleq \frac{g_{l,n}^{[\mathrm{m}]} \frac{\mathtt{M}_n}{\mathtt{M}_n+1} \mathtt{E}_n^{[\mathrm{m}]}}{\sum_{j\in\mathcal{A}(n)} \rho_{nj}(\mathcal{C})\, g_{l,j}^{[\mathrm{m}]} \frac{\mathtt{M}_j}{\mathtt{M}_j+1} \mathtt{E}_j^{[\mathrm{m}]} + N_0}, \quad (23)$$

where parameter $\rho_{nj}(\mathcal{C})$ is inversely proportional to the assigned subcarrier frequencies separation between tag n and tag $j \in \mathcal{A}(n)$ [1]. It depends on the spectral efficiency of the specific binary modulation implemented at each tag and the filtering functions at the reader:

$$\rho_{nj}(\mathcal{C}) = \max_{i_n, i_j \in \mathbb{B}} \left\{ \left[\varepsilon_{n,j} \left| F_{n,i_n}^{\mathcal{C}} - F_{j,i_j}^{\mathcal{C}} \right| \right]^{-2} \right\},\ j \in \mathcal{A}(n), \quad (24)$$

where $F_{n,i_n}^{\mathcal{C}}$ is the subcarrier frequency allocated under assignment $\mathcal{C}$ at tag n for bit $i_n \in \mathbb{B}$; parameter $\varepsilon_{n,j}$ is a constant that depends on the modulation and pulse shaping used, as well as the mismatch between the clocks of tag n and j. Subcarrier frequency difference raised at the second power, as opposed to the fourth power, is due to the power spectral density of FSK implemented at each tag, as opposed to (continuous phase) MSK [1].

The average received SINR for any $(l,n) \in \mathcal{L} \times \mathcal{N}$ can be expressed as:

$$\begin{aligned} \mathtt{SINR}_n^{[\mathrm{m}]}(\mathcal{C}) &= \frac{\mathbb{E}\left[g_{l,n}^{[\mathrm{m}]}\right] \frac{\mathtt{M}_n}{\mathtt{M}_n+1} \mathtt{E}_n^{[\mathrm{m}]}}{\sum_{j\in\mathcal{A}(n)} \rho_{nj}(\mathcal{C})\, \mathbb{E}\left[g_{l,j}^{[\mathrm{m}]}\right] \frac{\mathtt{M}_j}{\mathtt{M}_j+1} \mathtt{E}_j^{[\mathrm{m}]} + N_0} \\ &= \frac{\mathtt{E}_n^{[\mathrm{m}]}}{\sum_{j\in\mathcal{A}(n)} \rho_{nj}(\mathcal{C})\, \mathtt{E}_j^{[\mathrm{m}]} + N_0}. \end{aligned} \quad (25)$$

Proposition 3: For fixed monostatic topology and given subcarrier frequency assignment $\mathcal{C}$, under Rayleigh fading, i.e., $\mathtt{M}_n = 1$, outage probability for specific tag n and given slot $l \in \mathcal{L}$, is upper bounded as follows:

$$\mathbb{P}\left(\mathrm{SINR}_{l,n}^{[\mathrm{m}]}(\mathcal{C}) \leq \theta\right) \leq 1 - \mathtt{e}^{-\sqrt{\frac{2\theta}{\mathtt{SINR}_n^{[\mathrm{m}]}(\mathcal{C})}}}. \quad (26)$$

Proof: See Appendix C. ∎

It is emphasized that the above outcome depends on both tag location and network topology (through $\mathtt{E}_n^{[\mathrm{m}]}$), as well as subcarrier frequency assignment $\mathcal{C}$ (through parameter $\rho(\mathcal{C})$ above).

B. Multistatic

For given subcarrier frequency channel assignment $\mathcal{C}$, the instantaneous SINR of tag n for the l-th time slot is

$$\mathrm{SINR}_{l,n}^{[\mathrm{b}]}(\mathcal{C}) \triangleq \frac{g_{l,n}^{[\mathrm{b}]}\, \mathtt{E}_{l,n}^{[\mathrm{b}]}}{\sum_{j\in\mathcal{A}(n)} \rho_{nj}(\mathcal{C})\, g_{l,j}^{[\mathrm{b}]}\, \mathtt{E}_{l,j}^{[\mathrm{b}]} + N_0}. \quad (27)$$

The average SINR for multistatic case for any $(l,n) \in \mathcal{L} \times \mathcal{N}$ is given by:

$$\mathtt{SINR}_{l,n}^{[\mathrm{b}]}(\mathcal{C}) = \frac{\mathtt{E}_{l,n}^{[\mathrm{b}]}}{\sum_{j\in\mathcal{A}(n)} \rho_{nj}(\mathcal{C})\, \mathtt{E}_{l,j}^{[\mathrm{b}]} + N_0}. \quad (28)$$

Proposition 4: For fixed multistatic topology and subcarrier frequency assignment $\mathcal{C}$, under Rayleigh fading, i.e., $\mathtt{M}_{ln} = \mathtt{M}_n = 1$, the outage probability for specific tag n and a given slot $l \in \mathcal{L}$, is upper bounded as follows:

$$\begin{aligned} &\mathbb{P}\left(\mathrm{SINR}_{l,n}^{[\mathrm{b}]}(\mathcal{C}) \leq \theta\right) \\ &\qquad \leq 1 - 2\sqrt{\frac{\theta}{\mathtt{SINR}_{l,n}^{[\mathrm{b}]}(\mathcal{C})}}\, \mathsf{K}_1\left(2\sqrt{\frac{\theta}{\mathtt{SINR}_{l,n}^{[\mathrm{b}]}(\mathcal{C})}}\right), \end{aligned} \quad (29)$$

where $\mathsf{K}_1(\cdot)$ is the first order modified Bessel function of the second kind [32, eq. 10.27.3)].

Proof: The proof is provided in Appendix D. ∎

It is noted again that the above bound depends on tag location and network topology (through $\mathtt{E}_{l,n}^{[\mathrm{b}]}$), subcarrier frequency assignment $\mathcal{C}$ (through parameter $\rho(\mathcal{C})$ above) and slot l (in contrast to the monostatic case), since different CE per slot may be assumed.

V. Diversity Reception & Randomized Topologies

A. Diversity Reception

For channel realizations changing independently among different slots, i.e., if $g_{l,n}$ and $g_{l',n}$ are statistically independent for any $l \neq l' \in \mathcal{L}$, in addition to the assumptions followed so far, the following corollary regarding BER is relevant:

Corollary 1: When each tag scatters the same information across the L slots, BER for Rayleigh fading at the high SNR regime drops with $1/\mathrm{SNR}^d$, where $d \geq L$ and $d = L/2$ for the multistatic and monostatic architecture, respectively.

Proof: This stems from Propositions 1, 2 at Section III. ∎

Diversity receiver could exploit channel estimation and maximum ratio combining of the received SNRs across the L slots (coherent case) or selecting the maximum SNR across L slots and performing detection there (noncoherent case).

Diversity reception can be also applied in outage processing, briefly outlined below. For a fixed subcarrier frequency assignment $\mathcal{C}$, the monostatic information outage event for the n-th tag over L attempts (time slots) is the probability that n-th tag's SINR is below threshold θ over all L slots, i.e.,

$$\mathbb{P}\left(\bigcap_{l=1}^{L}\left\{\mathrm{SINR}_{l,n}^{[\mathrm{m}]}(\mathcal{C}) \leq \theta\right\}\right) \overset{(a)}{=} \left[\mathbb{P}\left(\mathrm{SINR}_{l,n}^{[\mathrm{m}]}(\mathcal{C}) \leq \theta\right)\right]^L \quad (30)$$

$$\overset{(b)}{\leq} \left(1 - \mathtt{e}^{-\sqrt{\frac{2\theta}{\mathtt{SINR}_n^{[\mathrm{m}]}(\mathcal{C})}}}\right)^L, \quad (31)$$

where (a) is due to the fact that $\{g_{l,n}^{[\mathrm{m}]}\}_{l\in\mathcal{L}}$ are IID across different l and (b) holds only under Rayleigh fading due to Eq. (26).

Similarly to the monostatic case, for fixed subcarrier frequency assignment $\mathcal{C}$ and given threshold θ, the multistatic information outage probability of tag n operating over L time slots is

$$\mathbb{P}\left(\bigcap_{l=1}^{L}\left\{\mathrm{SINR}_{l,n}^{[\mathrm{b}]}(\mathcal{C})\leq\theta\right\}\right)\overset{(a)}{=}\prod_{l=1}^{L}\mathbb{P}\left(\mathrm{SINR}_{l,n}^{[\mathrm{b}]}(\mathcal{C})\leq\theta\right) \tag{32}$$

$$\overset{(b)}{\leq}\prod_{l=1}^{L}\left(1-2\sqrt{\frac{\theta}{\mathtt{SINR}_{l,n}^{[\mathrm{b}]}(\mathcal{C})}}\,\mathsf{K}_1\left(2\sqrt{\frac{\theta}{\mathtt{SINR}_{l,n}^{[\mathrm{b}]}(\mathcal{C})}}\right)\right), \tag{33}$$

where (a) exploited the independence of $\left\{\mathrm{SINR}_{l,n}^{[\mathrm{b}]}(\mathcal{C})\right\}_{l\in\mathcal{L}}$ across different l and (b) holds only in a Rayleigh fading scenario due to Eq. (29).

B. Average Probability Over Random Square Grids

In order to obtain topology-independent outage probabilities, expressions that average over possible topologies have to be obtained, in order to average out the impact of the studied topology. While there are infinite classes of topologies to choose, our attention is restricted to the class of square $M\times M$ grid network topologies, which have simple two-dimensional (2D) representation and are easy to work with. For simplicity, it is assumed that grid resolution Δ, determining the granularity of the square grid, divides M, i.e., $M/\Delta=K\in\mathbb{N}$ and the set of 2D square grid points is denoted as follows:

$$\mathcal{G}_{M,\Delta}=\left\{[k_1\Delta\quad k_2\Delta]^{\top}:(k_1,k_2)\in\{0,1,\ldots,K\}^2\right\}. \tag{34}$$

Set $\mathcal{G}_{M,\Delta}$ has $(K+1)^2$ elements (2D grid points) and M, Δ are chosen such that $(K+1)^2\geq N+L+1$, i.e., possible tag locations are more than the total number of tags, emitters and reader. It is noticed that the larger the grid resolution is the more accurate becomes the evaluation of any studied outage metric.

For a monostatic architecture with fixed SDR reader's position $\mathbf{u}_{\mathrm{R}}\in\mathcal{G}_{M,\Delta}$, there are $\mathtt{J}_{K,N}^{[\mathrm{m}]}\triangleq\binom{(K+1)^2-1}{N}$ ways to place N tags in $\mathcal{G}_{M,\Delta}\backslash\{\mathbf{u}_{\mathrm{R}}\}$.[6] This is the ensemble of admissible square grid monostatic topologies. The calculation of a topology-independent average outage probabilities requires averaging over all $\mathtt{J}_{K,N}^{[\mathrm{m}]}$ possible topologies. Because $\mathtt{J}_{K,N}^{[\mathrm{m}]}$ is practically enormous, especially for large K, the averaging in this work is applied through Monte-Carlo, i.e., for a relatively large number of times, the following experiment is repeated: uniformly and random select a topology $\mathcal{T}_L^{[\mathrm{m}]}$ from the ensemble of monostatic grid topologies (i.e., each of them has probability $1/\mathtt{J}_{K,N}^{[\mathrm{m}]}$) and estimate the outage probability for the sampled topology. Finally, averaging is applied over the sampled topologies. The same methodology is applied to a multistatic architecture with L CEs and a single SDR reader, where $\mathtt{J}_{K,L,N}^{[\mathrm{b}]}\triangleq\binom{(K+1)^2-1-L}{N}=\binom{K^2+2K-L}{N}$ topologies exist, under the same assumption. Although the idea of averaging out over the ensemble of square grid topologies cannot offer closed-form, expressions, it provides a simple, yet tractable method to evaluate any tag-topology-independent metric of interest through Monte Carlo.

[6]If the ordering of how they are placed is not considered and the reader location is fixed.

VI. Energy Outage Probability for Passive Tags With RF Energy Harvesting

In contrast to the semi-passive tags assumed so far, passive tags do not have a dedicated (ambient or not) energy source. Instead, passive tags harvest RF energy from the illuminating carrier(s). For completeness, this section extends the comparison of monostatic vs multistatic architectures with passive tags.

For fixed position of CE, tag n and SDR reader at the l-th time slot, the *input* power at the RF harvesting circuit of tag n is given by:

$$P_{\mathrm{h},l,n}^{[\mathrm{m}]}=P_{\mathrm{R}}\,\mathsf{L}_{\mathrm{T}_n\mathrm{R}}\,(a_{l,\mathrm{T}_n\mathrm{R}})^2, \tag{35}$$

$$P_{\mathrm{h},l,n}^{[\mathrm{b}]}=P_{\mathrm{C}_l}\,\mathsf{L}_{\mathrm{C}_l\mathrm{T}_n}\,(a_{l,\mathrm{C}_l\mathrm{T}_n})^2, \tag{36}$$

for monostatic and multistatic architecture, respectively. Energy outage (EO) event at tag n occurs when for all L time slots the received input power at tag n RF circuitry is below a threshold θ_{h}, which models: a) the sensitivity of the RF harvesting circuit (i.e., the fact that RF harvesters offer zero power when input power is below a threshold) and b) the fact that all circuits require a specific minimum power to operate.[7] Thus, the EO event is defined as follows:

$$\mathbb{P}\left(\mathrm{EO}_{L,n}^{[\mathrm{m}]}\,|\theta_{\mathrm{h}}\right)\triangleq\mathbb{P}\left(\bigcap_{l=1}^{L}\left\{P_{\mathrm{h},l,n}^{[\mathrm{m}]}\leq\theta_{\mathrm{h}}\right\}\right), \tag{37}$$

$$\mathbb{P}\left(\mathrm{EO}_{L,n}^{[\mathrm{b}]}\,|\theta_{\mathrm{h}}\right)\triangleq\mathbb{P}\left(\bigcap_{l=1}^{L}\left\{P_{\mathrm{h},l,n}^{[\mathrm{b}]}\leq\theta_{\mathrm{h}}\right\}\right), \tag{38}$$

for monostatic and multistatic architecture, respectively. Network topology impact on the energy outage probabilities for multistatic and monostatic systems is present due to the path-gains $\{\mathsf{L}_{\mathrm{C}_l\mathrm{T}_n}\}_{l\in\mathcal{L}}$ and $\mathsf{L}_{\mathrm{T}_n\mathrm{R}}$.

For the monostatic architecture, RVs $\{P_{\mathrm{h},l,n}^{[\mathrm{m}]}\}_{l\in\mathcal{L}}$ are IID and each $P_{\mathrm{h},l,n}^{[\mathrm{m}]}$ is Gamma RV with parameters $\left(\mathtt{M}_n,\frac{P_{\mathrm{R}}\mathsf{L}_{\mathrm{T}_n\mathrm{R}}}{\mathtt{M}_n}\right)$ and cumulative distribution function (CDF) given in [38, Table I]; the monostatic energy outage event in (37) is given by:

$$\mathbb{P}\left(\mathrm{EO}_{L,n}^{[\mathrm{m}]}\,|\theta_{\mathrm{h}}\right)=\left(\frac{\gamma\left(\mathtt{M}_n,\frac{\mathtt{M}_n\theta_{\mathrm{h}}}{P_{\mathrm{R}}\mathsf{L}_{\mathrm{T}_n\mathrm{R}}}\right)}{\Gamma(\mathtt{M}_n)}\right)^{L}, \tag{39}$$

where $\gamma(a,x)=\int_0^x t^{a-1}\mathrm{e}^{-t}\mathrm{d}t$ is the lower incomplete gamma function.

For the multistatic architecture, $P_{\mathrm{h},l,n}^{[\mathrm{b}]}$ is a Gamma RV with parameters $\left(\mathtt{M}_{ln},\frac{P_{\mathrm{C}_l}\mathsf{L}_{\mathrm{C}_l\mathrm{T}_n}}{\mathtt{M}_{ln}}\right)$ and RVs $\{P_{\mathrm{h},l,n}^{[\mathrm{b}]}\}_{l\in\mathcal{L}}$ are independent; as a result, the energy outage event in (38) is

[7]State-of-the-art passive RFID tags exhibit $\theta_{\mathrm{h}}=-22$ dBm [37].

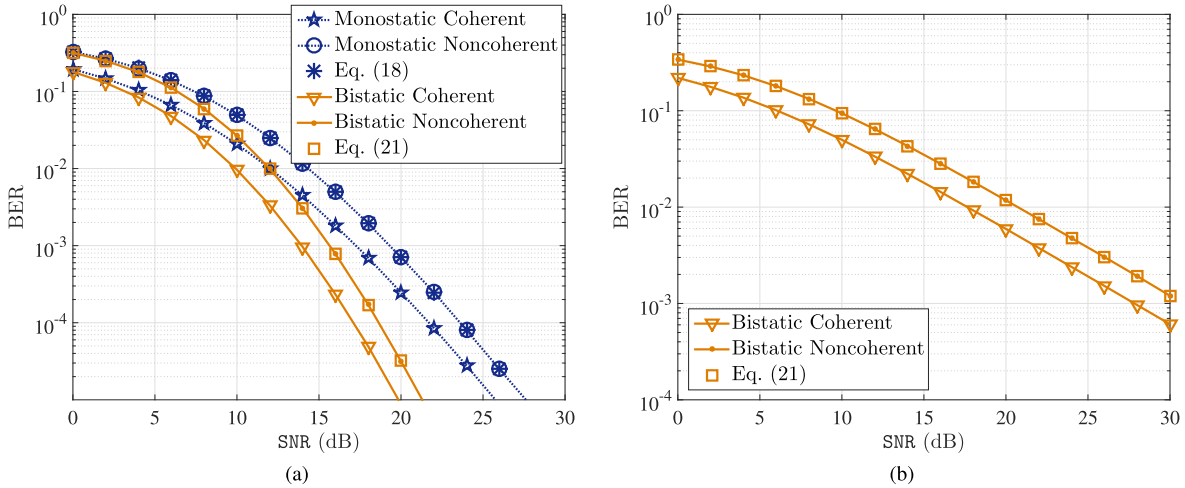

Fig. 4. Left (Right): Monostatic vs bistatic BER versus SNR for ML coherent and noncoherent detection and Nakagami fading with parameters $\mathtt{M}_n = 5.7619$, $\mathtt{M}_{ln} = 5.2632$ ($\mathtt{M}_{ln} = 1, \mathtt{M}_n = 5.7619$, assuming a NLoS CE-to-tag scenario).

calculated as follows:

$$\mathbb{P}\left(\mathrm{EO}_{L,n}^{[\mathrm{b}]}\left|\theta_{\mathrm{h}}\right.\right) = \prod_{l=1}^{L} \frac{\gamma\left(\mathtt{M}_{ln}, \frac{\mathtt{M}_{ln}\theta_{\mathrm{h}}}{P_{\mathrm{C}_l}\mathtt{L}_{\mathrm{C}_l\mathrm{T}_n}}\right)}{\Gamma\left(\mathtt{M}_{ln}\right)}. \tag{40}$$

The average across all tags energy outage event is by taking the average of Eqs. (37) and (38) across all tags, i.e.,

$$\frac{1}{N}\sum_{n=1}^{N}\mathbb{P}\left(\mathrm{EO}_{L,n}^{[\mathrm{m}]}\left|\theta_{\mathrm{h}}\right.\right),\ \frac{1}{N}\sum_{n=1}^{N}\mathbb{P}\left(\mathrm{EO}_{L,n}^{[\mathrm{b}]}\left|\theta_{\mathrm{h}}\right.\right). \tag{41}$$

Another important metric that measures the worst-case energy outage is the maximum energy outage across all tags, i.e.,

$$\max_{n\in\mathcal{N}}\left\{\mathbb{P}\left(\mathrm{EO}_{L,n}^{[\mathrm{m}]}\left|\theta_{\mathrm{h}}\right.\right)\right\},\ \max_{n\in\mathcal{N}}\left\{\mathbb{P}\left(\mathrm{EO}_{L,n}^{[\mathrm{b}]}\left|\theta_{\mathrm{h}}\right.\right)\right\}. \tag{42}$$

It is emphasized again that the above outage probabilities depend on a specific multistatic or monostatic WSN topology. Energy outage expressions that are topology-independent can be offered using averaging over the ensemble of square grid topologies as in Section V-B.

VII. Simulation Results

First we study the BER performance of monostatic and bistatic systems, for $L = 1$ slot and $N = 1$ tag. Rician fading parameters $\kappa_n = 10$ and $\kappa_{ln} = 9$ are considered, setting $\mathtt{M}_n = \frac{(\kappa_n+1)^2}{2\kappa_n+1} = 5.7619$ and $\mathtt{M}_{ln} = \frac{(\kappa_{ln}+1)^2}{2\kappa_{ln}+1} = 5.2632$. Fig. 4a illustrates the exact BER performance under coherent and noncoherent reception for the two scatter radio architectures. Common $\mathtt{SNR} = \mathtt{SNR}_{l,n}^{[\mathrm{b}]} = \mathtt{SNR}_{n}^{[\mathrm{m}]}$ is assumed, resulting to monostatic reader transmission power P_{R} and bistatic carrier emitter power P_{C_l} related according to Eqs. (9), (14) $\left(P_{\mathrm{R}} = \frac{\mathtt{L}_{\mathrm{C}_l,\mathrm{T}_n}}{\mathtt{L}_{\mathrm{T}_n,\mathrm{R}}}\frac{\mathtt{M}_n P_{\mathrm{C}_l}}{\mathtt{M}_n+1}\right)$. Any monostatic or bistatic topology offering the specific SNR is applicable to this plot. Upper bounds derived in Eq. (18) and Eq. (21) are also plotted. It can be seen that the bistatic architecture outperforms the monostatic and high-SNR slope is clearly different among the two architectures, as expected. It can be also seen that the derived upper bounds for coherent detection schemes coincide with the curves of noncoherent detection.

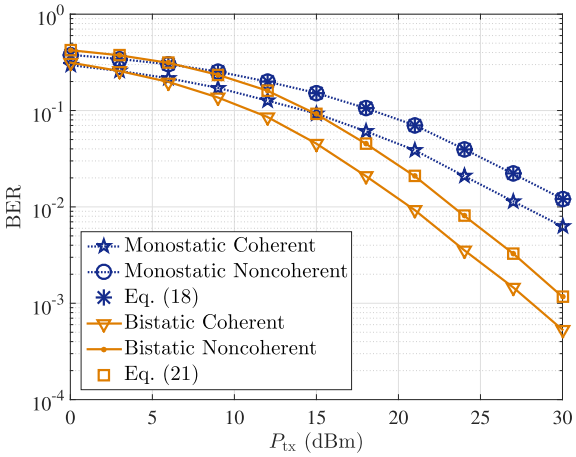

Fig. 5. Monostatic vs bistatic BER performance versus P_{tx} in a 40×40 topology for ML coherent and noncoherent detection averaged over random tag locations.

TABLE I
Noise and Tag Parameters

$N_0 = -169$ dBm/Hz	$F_{\mathrm{c}} = 868$ MHz	$\lambda = \frac{3\cdot 10^8}{F_{\mathrm{c}}}$ m
$\lvert\Gamma_{n,0} - \Gamma_{n,1}\rvert = 2, \forall n$	$\mathtt{s}_n = 0.1, \forall n$	

Fig. 4b studies the BER performance as a function of SNR for a scenario where the tag is far-away from CE (possibly a few kilometers) but the tag-to-reader distance is relatively small (a few feet). This is a Rayleigh-Nakagami (Rice) scenario, that could be the case when the tag is illuminated by broadcasting stations and the receiver is close to the tag. In such scenario, the monostatic architecture is not applicable. Due to the large CE-to-tag distance, the link from CE-to-tag is assumed NLoS, i.e., $\kappa_{ln} = 0$ and thus $\mathtt{M}_{ln} = \frac{(\kappa_{ln}+1)^2}{2\kappa_{ln}+1} = 1$, while tag-to-reader is assumed strong LoS, thus $\kappa_n = 10$ with $\mathtt{M}_n = \frac{(\kappa_n+1)^2}{2\kappa_n+1} = 5.7619$. In such extreme case, where the monostatic architecture cannot be defined, the bistatic BER is less than 1% for received SNR values less than 17 dB (20 dB) under coherent (noncoherent) detection. The above demonstrate the potential benefits and flexibility of bistatic architecture in cases where CE is far away from tag.

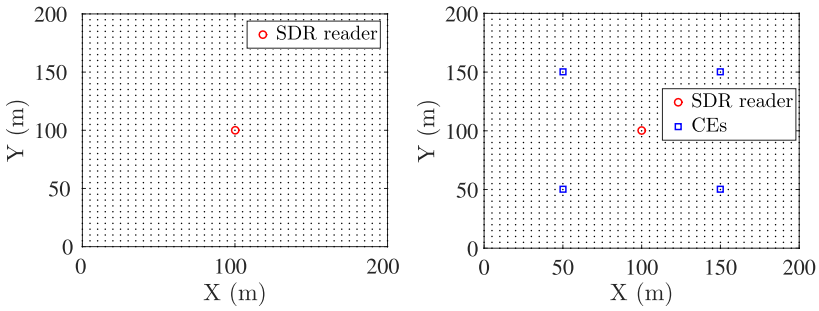

(a) Monostatic topology (b) Multistatic topology with 4 CEs.

Fig. 6. Network setup: Grid points (dots) are possible tag locations.

Fig. 5 studies the impact of transmit power on BER for random tag locations. An SDR reader and a CE are placed in positions $[0\ 0]^\top$ and $[40\ 40]^\top$, respectively, while the position of tag follows uniform distribution over a 40×40 m^2 topology. Common transmit power is used for fair comparison for monostatic and bistatic architectures, i.e., $P_{\rm tx}=P_{\rm R}=P_{{\rm C}_l}$. For each sampled tag location the small scale fading parameters change as $\kappa_n\sim\mathcal{U}[0,20]$ and $\kappa_{ln}\sim\mathcal{U}[0,20]$, setting $\mathtt{M}_n=\frac{(\kappa_n+1)^2}{2\kappa_n+1}$ and $\mathtt{M}_{ln}=\frac{(\kappa_{ln}+1)^2}{2\kappa_{ln}+1}$. In addition, the path-loss exponents (PLEs) from CE-to-tag and SDR reader-to-tag are $\mathcal{U}[2,2.5]$. The noise- and tag-related parameters are shown in Table I. It can be seen that the average BER performance of a randomly placed tag (evaluated over several possible tag locations) is smaller in the bistatic architecture. It is also observed that the BER decay is faster in the bistatic compared to the monostatic architecture, corroborating the diversity gains offered by the bistatic system.

For grid WSN topologies of size $M\times M$ m^2 and grid resolution Δ m, energy and information outage are examined, using $M=2.5$, $\Delta=0.125$ and $M=200$, $\Delta=5$, respectively. For information (energy) outage simulations, random tag topologies are generated from $\mathcal{G}_{200,5}$ ($\mathcal{G}_{2.5,0.125}$) consisting of N tags, $L=4$ CEs placed at $\{\mathbf{u}_{{\rm C}_l}\}_{l=1}^4=\{[\frac{M}{4}\ \ \frac{M}{4}]^\top,[\frac{3M}{4}\ \ \frac{M}{4}]^\top,[\frac{3M}{4}\ \ \frac{3M}{4}]^\top,[\frac{M}{4}\ \ \frac{3M}{4}]^\top\}$ for multistatic system, and an SDR reader placed at $[\frac{M}{2}\ \ \frac{M}{2}]$ (i.e., middle of the topology), in order to maximize the coverage. The grid topology utilized in information outage simulations is depicted in Figs. 6a and 6b for the monostatic and multistatic architectures, respectively. Similar with previous paragraph noise/tag-related parameters are considered (Table I). After sampling the grid topology, random PLEs $\nu_{ln}\sim\mathcal{U}[2,2.5]$ and $\nu_n\sim\mathcal{U}[2,2.5]$ are generated for link from l-th CE to n-th tag and link from n-th tag to SDR reader, respectively. In addition, to offer robustness against channel fading, after sampling the topology in the Nakagami fading scenarios, Nakagami parameters are randomly generated as follows: $\mathtt{M}_{ln}\sim\mathcal{U}[1,5]$ and $\mathtt{M}_n\sim\mathcal{U}[1,5]$, for link from l-th CE to n-th tag and link from n-th tag to SDR reader, respectively. For a fair comparison, equal transmission power for monostatic and multistatic architecture is utilized, setting $P_{\rm tx}=P_{\rm R}=P_{{\rm C}_l},\forall l\in\mathcal{L}$.

Considering a passive-tag WSN scenario, Fig. 7 examines the topology-independent average and maximum energy outage probability (by averaging Eqs. (41) and (42) over several sampled grid topologies), as a function of harvesting threshold $\theta_{\rm h}$ under Nakagami fading, with $P_{\rm tx}=35$ dBm and $N=8$ tags. It is noted that the probability for a tag to be placed near a CE is higher in the multistatic architecture and thus, energy outage events are more frequent in the monostatic architecture. Energy outage is a performance bound for WSNs consisting of passive tags, since harvesting adequate energy is necessary before any other tag operation, including backscattering. It is remarked that for energy outage probability of 10%, the multistatic architecture outperforms the monostatic by 4.5 dB for average and maximum outage performance.

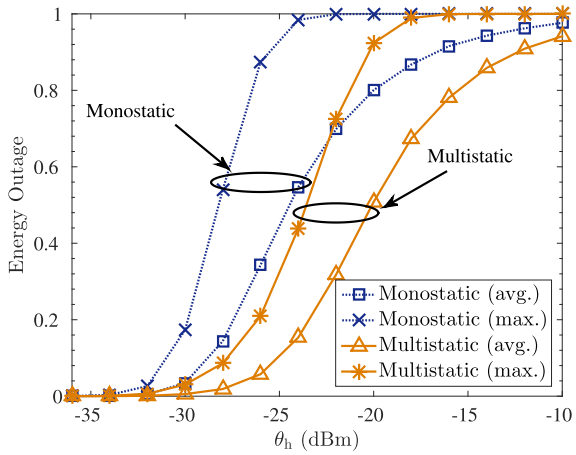

Fig. 7. Topology-independent average and maximum energy outage performance versus threshold $\theta_{\rm h}$ for monostatic and multistatic network of Fig. 6 using $\mathcal{G}_{2.5,0.125}$.

Finally, information outage is evaluated for a network of semi-passive tags. Since average outage probability expressions in Eqs. (30) and (32) do not admit a closed form, an extra Monte Carlo step is required. Specifically, for a given sampled topology, Rayleigh ($\mathtt{M}_n=\mathtt{M}_{ln}=1$) and Nakagami small-scale fading coefficients are generated, as well as a random subcarrier frequency assignment to the tags. For the sampled topology, we average out the impact of fading and frequency assignment over several random realizations to evaluate Eqs. (30) and (32) through Monte Carlo. The upper bounds for Rayleigh fading are evaluated directly through Eqs. (31) and (33) after sampling the topology. The above experiments are conducted for several sampled grid topologies to obtain topology-free expressions. For an allocation $\mathcal{C}$, the c-th frequency pair is assigned to tag n if $c=\mathsf{p}_{\mathcal{C}}(n)\in\mathcal{N}$,

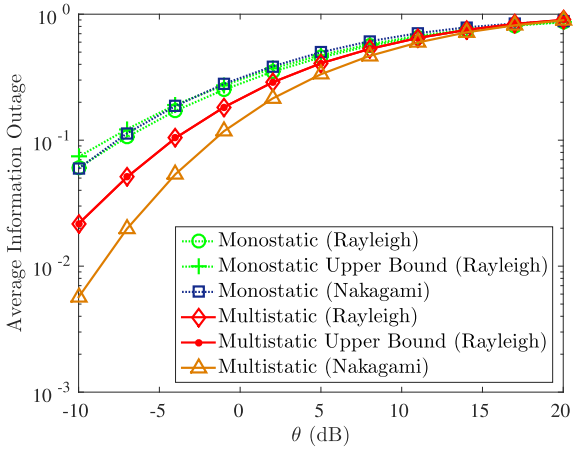

Fig. 8. Tag location-independent, average information outage probability versus threshold θ for monostatic and multistatic architecture of Fig. 6.

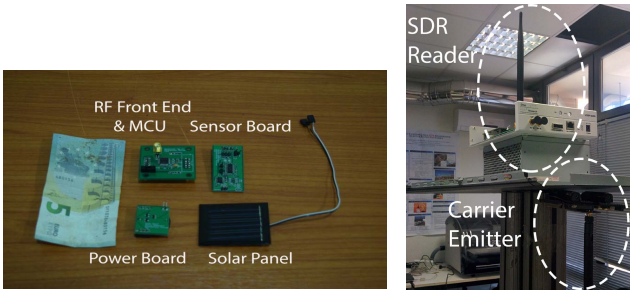

(a) Tag (b) Reader

Fig. 9. A prototype scatter radio tag (left) and a custom reader (right); the receiver antenna is on the top side of a metal box, while the carrier emitter (CE) is on the bottom side.

where $\mathsf{p}_{\mathcal{C}}$ denotes the permutation associated with a specific assignment $\mathcal{C}$. The following parameters are utilized: $T = 1$ msec (i.e., 1 Kbps bitrate), $\varepsilon_{n,j} = 2\pi T$ for all $n, j \in \mathcal{N}$ with $n \neq j$, and the subcarrier frequency pair for the n-th tag, $\{F^{\mathcal{C}}_{n,0}, F^{\mathcal{C}}_{n,1}\}$, is given by $F^{\mathcal{C}}_{n,0} = (0.1 + c\,F_{\rm sp})$ MHz and $F^{\mathcal{C}}_{n,1} = (0.1 + c\,F_{\rm sp} + F_{\rm sp}/5)$ MHz with $F_{\rm sp} = 0.01$ MHz, $c = 1, 2, \ldots, N$. Thus, for a given channel assignment $\mathcal{C}$, the coefficients in Eq. (24) for any pair of tags $(n, j) \in \mathcal{N} \times \mathcal{N}$, with $n \neq j$, can be expressed as $\rho_{nj}(\mathcal{C}) = \rho_{jn}(\mathcal{C}) = \frac{25}{[2\,\pi\,T\,(5|\mathsf{p}_{\mathcal{C}}(n) - \mathsf{p}_{\mathcal{C}}(j)| - 1)\,F_{\rm sp}]^2}$.

Fig. 8 illustrates the topology-independent average outage probability (as well as the corresponding upper bounds for Rayleigh fading) for monostatic and multistatic architectures, as a function of threshold θ, for $N = 100$ tags and $P_{\rm tx} = 28$ dBm. It is noted that the specific monostatic network setup (Fig. 6a) is the most appropriate among all possible choices of $\mathcal{G}_{200,5}$ in terms of coverage, since the SDR reader is located in the middle of the grid. Fig. 8 shows that for information outage 10% multistatic system outperforms monostatic by 3 dB in Rayleigh fading scenario, while for Nakagami fading the gap approaches 8 dB. The performance gap increases as threshold θ decreases. It can be also seen that the proposed bounds after averaging over all sampled tag locations are tight, especially for the multistatic architecture. It is clear again that the multistatic architecture offers higher reliability, as well as better coverage for scatter radio WSNs.

VIII. Experimental Results

Motivated by the above finding, a digital *multistatic* scatter radio sensor network is constructed [39], targeting environmental and agriculture applications for ultra low-cost, microclimate monitoring around each plant. The environmental quantities measured include air-humidity, soil moisture, temperature, which vary slowly with time and thus, low bitrate (1 Kbps) per sensor was adequate. Tags could communicate with the reader simultaneously, using receiver-less subcarrier (switching) frequency division multiple access (FDMA), as explained in Section II; the CEs transmitted with TDM access a CW at 13 dBm power and 868 MHz carrier frequency.

Each prototype tag consisted of two distinct boards, the communication and the power board (Fig. 9a). The communication board was responsible for the communication and sensing operations and included a 8-bit mixed-signal microcontroller unit (MCU) with analog-to-digital converter, a RF transistor and input/output (I/O) pins for sensors' inputs. Each tag utilized scatter radio binary FSK (BFSK) modulation; 30 distinct orthogonal subcarrier frequency pairs could be produced. In order to increase the total number of tags and sustain low-power operation, "sleep" mode was implemented in all tags, with random "wake up". Thus, multiple tags can share the same pair of subcarrier frequencies, increasing the total number of tags in the network, based on the utilized "sleep-scatter" duty cycle. Moreover, a $1/2$ rate Reed-Muller encoder was implemented at each MCU [17]. Finally, the tag operated with a small solar panel during the daytime and a small coin cell battery during the night. The battery can be easily replaced by a super capacitor at the power board [22], [23], [24].

Furthermore, in order to emulate a monostatic reader, the SDR reader and the CE were placed on the opposite sides of a metallic box. This structure provided good isolation between the transmit and the receive antennas, without using a circulator. The monostatic setup is depicted in Fig. 9b.

The outdoor measurement campaign consisted of two campaigns. In the first campaign, the maximum ranges of the tag-to-SDR links were found. The metric used to find the maximum range was tag BER at the receiver, up to 5%. The multistatic architecture achieved tag-to-SDR reader ranges over 140 m, with CE-to-tag range in the order of 10 m. The achieved ranges of the monostatic setup were one order of magnitude smaller than the multistatic, with maximum tag-to-SDR range in the order of 15 m.

In the second campaign, coverage was examined in a field of 3500 m^2 area. For the multistatic architecture two network topologies were deployed, one with three and one with four CEs. In the first topology (shown in Fig. 10a), the SDR reader was placed at one field corner, maximizing the tag-to-SDR reader distance, while the three CEs were placed around the field. In the second topology the reader was placed at the field center and the four CEs located as shown in Fig. 10b. For the monostatic architecture, multiple readers/CEs were deployed. Since the monostatic architecture's ranges were shorter, a total of eight readers were utilized, as shown in Fig. 10c. It is also noted that using only four monostatic SDR readers at the same locations, where CEs were placed in

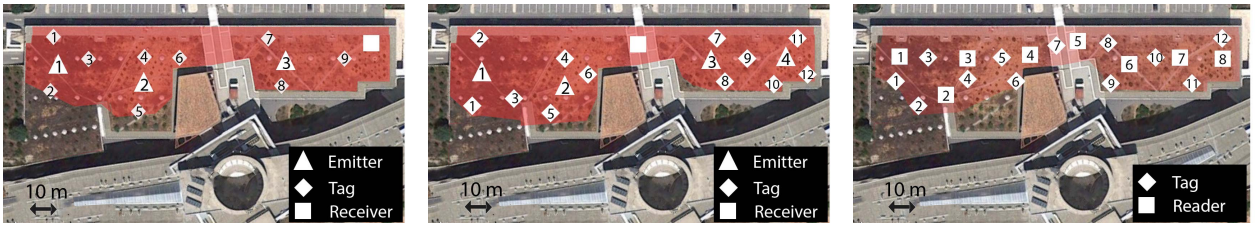

(a) Multistatic: receiver at the corner, 3 CEs. (b) Multistatic: receiver at the center, 4 CEs. (c) Monostatic: 8 readers.

Fig. 10. Multistatic and monostatic setup for measurement campaigns.

the multistatic case, would offer a smaller monostatic coverage of $4 \cdot \pi \cdot 15^2 = 2827$ m^2.

The second campaign showed that both architectures can cover similar areas, provided that the monostatic architecture utilizes additional readers, incurring higher monetary cost. In sharp contrast, the multistatic architecture is more flexible with greater range, even with a single SDR receiver but multiple low-cost CEs. Equivalently, with only one reader, the monostatic architecture would offer much smaller field coverage, compared to the multistatic, as clearly shown in Fig. 10a, Fig. 10b and Fig. 10c.

The methodology of this work can offer tag-topology-independent performance metric expressions accounting for the (random) spatial distribution of the tags over square grid topologies. Thus, the outcome of this work could assist in assessing appropriate topologies for CEs and reader installation points, with a simple, yet tractable way. Specifically, in order to design backscatter sensor networks with increased range, extended information or energy coverage, the following procedure can be applied: a) create a multistatic network consisting of a single reader placed in the middle of the topology and L carrier emitters (CEs) placed randomly over L grid points; fix the location of the CEs and exclude $L+1$ grid points from the set of grid points that could be assigned to the tags; b) evaluate and store a tag-topology-free value for the metric of interest (BER or average information outage or average/maximum energy outage), averaged with respect to the positions of the N tags over several realizations; c) repeat the above steps $T_{\max}$ times, by changing each time the position of the L CEs; d) among the $T_{\max}$ possible CE topologies, choose the one offering the smallest value for the metric of interest. In that way, the system designer can offer convincing arguments for specific installation topology of the reader and the CEs, exploiting the BER metric for flexible Nakagami or the outage probability metric for (worst-case) Rayleigh small-scale scaling. As a result, several multistatic topologies for the possible location of the CEs or the reader can be assessed, depending on the application scenario and the wireless environment assumptions. Future research could extend the analysis of this work, in either monostatic or multistatic backscatter architectures, incorporating specific, application-dependent spatial distributions for the tags' locations.

IX. Conclusion

It was clearly shown that the multistatic scatter radio architecture offers more reliable reception as well as better field coverage, while demonstrating smaller sensitivity to the topology of the tags, compared to the monostatic architecture. It is demonstrated under realistic Nakagami small-scale fading scenarios and path-loss models that not only the BER decay is doubled in multistatic architecture compared to monostatic one, but also, energy and information outage events are less frequent in multistatic systems due to the flexible morphology of the multistatic WSN architecture. This work offers a concrete proof that large-scale and reliable scatter radio networks can be implemented, with digital, bistatic principles, and low-power scatter radio sensors.

Appendix A
Proof of Proposition 1

For Rayleigh fading, i.e., $\mathtt{M}_n = 1$, RV $a_{l,n}^{[\mathrm{m}]} = \left(a_{l,\mathrm{T}_n\mathrm{R}}\right)^2$ follows exponential distribution. Using Eq. (17), the unconditional probability of error over the l-th slot for the n-th tag is given by:

$$\begin{aligned}\Pr\left(e_{l,n}^{[\mathrm{m}]}\right) &= \mathop{\mathbb{E}}_{a_{l,n}^{[\mathrm{m}]}}\left[\Pr\left(e_{l,n}^{[\mathrm{m}]} \mid a_{l,n}^{[\mathrm{m}]}\right)\right] \\ &= \int_0^{\infty} \mathtt{Q}\left(x\sqrt{\frac{\mathtt{SNR}_n^{[\mathrm{m}]}}{2}}\right)\mathtt{e}^{-x}\mathtt{d}x \\ &= \frac{1}{2} - \mathtt{e}^{\frac{1}{\mathtt{SNR}_n^{[\mathrm{m}]}}}\mathtt{Q}\left(\sqrt{\frac{2}{\mathtt{SNR}_n^{[\mathrm{m}]}}}\right), \end{aligned} \tag{43}$$

where [32, eqs. (7.14.2), (7.2.1), and (7.2.2)] are utilized. The diversity order for the probability of error in (43) is given by [40]:

$$\lim_{\mathtt{SNR}_n^{[\mathrm{m}]}\to\infty} \frac{\log\left(\Pr\left(e_{l,n}^{[\mathrm{m}]}\right)\right)}{\log\left(\mathtt{SNR}_n^{[\mathrm{m}]}\right)} = \lim_{x\to 0}\frac{\log\left(\frac{1}{2} - \mathtt{e}^{x}\,\mathtt{Q}\left(\sqrt{2x}\right)\right)}{\log\left(\frac{1}{x}\right)}.$$

By applying the rule of L'Hospital:

$$\lim_{x\to 0}\frac{-\mathtt{e}^{x}\mathtt{Q}\left(\sqrt{2\,x}\right) + \frac{1}{2\sqrt{\pi\,x}}}{-\frac{1}{x}\left[\frac{1}{2} - \mathtt{e}^{x}\,\mathtt{Q}\left(\sqrt{2\,x}\right)\right]} = \lim_{x\to 0}\frac{x\,\mathtt{Q}\left(\sqrt{2\,x}\right) - \frac{\mathtt{e}^{-x}\sqrt{x}}{2\sqrt{\pi}}}{\frac{\mathtt{e}^{-x}}{2} - \mathtt{Q}\left(\sqrt{2\,x}\right)}. \tag{44}$$

Applying again the rule of L'Hospital:

$$\lim_{x\to 0}\frac{\mathtt{Q}\left(\sqrt{2\,x}\right) - \frac{\mathtt{e}^{-x}}{4\sqrt{\pi x}}}{-\frac{\mathtt{e}^{-x}}{2} + \frac{\mathtt{e}^{-x}}{2\sqrt{\pi x}}} = \lim_{x\to 0}\frac{\mathtt{e}^{x}\sqrt{x}\,\mathtt{Q}\left(\sqrt{2\,x}\right) - \frac{1}{4\sqrt{\pi}}}{-\frac{\sqrt{x}}{2} + \frac{1}{2\sqrt{\pi}}} = -\frac{1}{2}. \tag{45}$$

APPENDIX B
PROOF OF PROPOSITION 2

For Rayleigh fading, i.e., $\mathtt{M}_{ln} = \mathtt{M}_n = 1$, with the aid of [32, eq. (13.6.6)], function $\mathsf{U}\left(1, 1, \frac{2}{\mathtt{SNR}_{l,n}^{[\mathrm{b}]}}\right) = \mathsf{e}^{\frac{2}{\mathtt{SNR}_{l,n}^{[\mathrm{b}]}}} \Gamma\left(0, \frac{2}{\mathtt{SNR}_{l,n}^{[\mathrm{b}]}}\right)$, where $\Gamma(a,x) \triangleq \int_x^\infty t^{a-1}\,\mathsf{e}^{-t}\mathsf{d}t$ is the upper incomplete gamma function. The diversity order for the upper bound becomes

$$\lim_{x\to\infty} \frac{\log\left(\frac{1}{x}\,\mathsf{e}^{\frac{2}{x}}\,\Gamma\big(0,\frac{2}{x}\big)\right)}{\log(x)} = \lim_{x\to\infty}\left[\frac{\log\left(\frac{1}{x}\right)}{\log(x)} + \frac{\log\left(\mathsf{e}^{\frac{2}{x}}\right)}{\log(x)} + \frac{\log\left(\Gamma\big(0,\frac{2}{x}\big)\right)}{\log(x)}\right]. \quad (46)$$

By applying the L'Hospital's rule and [32, eq. (8.8.13)]:

$$\lim_{x\to\infty}\left[\frac{\log\left(\frac{1}{x}\right)}{\log(x)} + \frac{2}{x\log(x)} + \frac{\mathsf{e}^{-\frac{2}{x}}}{\Gamma\left(0,\frac{2}{x}\right)}\right] = -1 + \lim_{x\to\infty}\frac{\mathsf{e}^{-\frac{2}{x}}}{\Gamma\big(0,\frac{2}{x}\big)} = -1, \quad (47)$$

where $\lim_{x\to\infty}\frac{\log\left(\frac{1}{x}\right)}{\log(x)} = -1$, $\lim_{x\to\infty}\frac{2}{x\log(x)} = 0$ and $\lim_{x\to\infty}\frac{\mathsf{e}^{-\frac{2}{x}}}{\Gamma\left(0,\frac{2}{x}\right)} = \lim_{x\to 0}\frac{1}{\Gamma(0,2x)} = 0$, due to [32, eqs. (8.4.4) and (6.6.2)].

APPENDIX C
PROOF OF PROPOSITION 3

The PDF of RV $g_{l,n}^{[\mathrm{m}]} \triangleq \left(a_{l,n}^{[\mathrm{m}]}\right)^2 = \left(a_{l,\mathrm{T}_n\mathrm{R}}\right)^4$ can be determined through RV $a_{l,n}^{[\mathrm{m}]} = \left(a_{l,\mathrm{T}_n\mathrm{R}}\right)^2$, which follows Gamma distribution with PDF given in Eq. (16). Using the formula in [30, p. 199], the required PDF for $x \geq 0$ is

$$\mathsf{f}_{g_{l,n}^{[\mathrm{m}]}}(x) = \frac{1}{2\sqrt{x}}\mathsf{f}_{a_{l,n}^{[\mathrm{m}]}}(\sqrt{x}) = (\mathtt{M}_n)^{\mathtt{M}_n}\,\frac{x^{\frac{\mathtt{M}_n}{2}-1}}{2\,\Gamma(\mathtt{M}_n)}\,\mathsf{e}^{-\mathtt{M}_n\sqrt{x}}. \quad (48)$$

For Rayleigh fading, i.e., $\mathtt{M}_n = 1$ in Eq. (48), the PDF of RV $g_{l,n}^{[\mathrm{m}]}$ is simplified to $\mathsf{f}_{g_{l,n}^{[\mathrm{m}]}}(x) = \frac{1}{2\sqrt{x}}\mathsf{e}^{-\sqrt{x}}$, $x \geq 0$. The corresponding cumulative distribution function (CDF) is given by

$$\mathsf{F}_{g_{l,n}^{[\mathrm{m}]}}(x) = \int_0^x \mathsf{f}_{g_{l,n}^{[\mathrm{m}]}}(y)\,\mathsf{d}y = 1 - \mathsf{e}^{-\sqrt{x}}, \quad x \geq 0. \quad (49)$$

The monostatic outage probability for $\mathtt{M}_n = 1$ follows:

$$\mathbb{P}\Big(\mathrm{SINR}_{l,n}^{[\mathrm{m}]}(\mathcal{C}) \leq \theta\Big) \overset{(a)}{=} \mathbb{P}\left(g_{l,n}^{[\mathrm{m}]} \leq \frac{2\,\theta\,N_0}{\mathtt{E}_n^{[\mathrm{m}]}} + \frac{\theta\,\mathrm{I}_{l,n}^{[\mathrm{m}]}(\mathcal{C})}{\mathtt{E}_n^{[\mathrm{m}]}}\right)$$
$$\overset{(b1)}{=} \underset{\mathrm{I}_{l,n}^{[\mathrm{m}]}(\mathcal{C})}{\mathbb{E}}\left[\mathsf{F}_{g_{l,n}^{[\mathrm{m}]}|\mathrm{I}_{l,n}^{[\mathrm{m}]}(\mathcal{C})}\left(\frac{2\,\theta\,N_0}{\mathtt{E}_n^{[\mathrm{m}]}} + \frac{\theta\,\mathrm{I}_{l,n}^{[\mathrm{m}]}(\mathcal{C})}{\mathtt{E}_n^{[\mathrm{m}]}}\right)\right]$$
$$\overset{(b2)}{=} \underset{\mathrm{I}_{l,n}^{[\mathrm{m}]}(\mathcal{C})}{\mathbb{E}}\left[\mathsf{F}_{g_{l,n}^{[\mathrm{m}]}}\left(\frac{2\,\theta\,N_0}{\mathtt{E}_n^{[\mathrm{m}]}} + \frac{\theta\,\mathrm{I}_{l,n}^{[\mathrm{m}]}(\mathcal{C})}{\mathtt{E}_n^{[\mathrm{m}]}}\right)\right] \quad (50)$$
$$\overset{(c)}{\leq} \mathsf{F}_{g_{l,n}^{[\mathrm{m}]}}\left(\frac{2\,\theta\,N_0}{\mathtt{E}_n^{[\mathrm{m}]}} + \frac{\theta\,\mathbb{E}\left[\mathrm{I}_{l,n}^{[\mathrm{m}]}(\mathcal{C})\right]}{\mathtt{E}_n^{[\mathrm{m}]}}\right)$$
$$\overset{(d)}{=} \mathsf{F}_{g_{l,n}^{[\mathrm{m}]}}\left(\frac{2\,\theta}{\mathtt{SINR}_n^{[\mathrm{m}]}(\mathcal{C})}\right) = 1 - \mathsf{e}^{-\sqrt{\frac{2\theta}{\mathtt{SINR}_n^{[\mathrm{m}]}(\mathcal{C})}}}. \quad (51)$$

In (a), total interference at tag n for the monostatic system at the l-th time slot was defined as $\mathrm{I}_{l,n}^{[\mathrm{m}]}(\mathcal{C}) \triangleq \sum_{j\in\mathcal{A}(n)}\rho_{nj}(\mathcal{C})\,g_{l,j}^{[\mathrm{m}]}\,\mathtt{E}_j^{[\mathrm{m}]}$; step $(b1)$ exploited the law of iterated expectation [41]; step $(b2)$ exploited the assumed statistical independence between $g_{l,n}^{[\mathrm{m}]}$ and $g_{l,j}^{[\mathrm{m}]}$ for any $j \neq n$; step (c) utilized Jensen's inequality, taking into account the concavity of CDF in Eq. (49); (d) exploited the linearity of expectation, the SINR definition in Eq. (25), and $\mathtt{M}_n = 1$.

APPENDIX D
PROOF OF PROPOSITION 4

Proof of Eq. (29) is along the same lines with proof in Proposition 3. The CDF of $g_{l,n}^{[\mathrm{b}]}$ for Rayleigh fading is needed, as well as proof of its concavity. Using $\mathtt{M}_{ln} = \mathtt{M}_n = 1$ in Eq. (19), the PDF is simplified to $\mathsf{f}_{g_{l,n}^{[\mathrm{b}]}}(x) = 2\,\mathsf{K}_0(2\sqrt{x})$, $x \geq 0$. The corresponding CDF can be calculated as follows:

$$\mathsf{F}_{g_{l,n}^{[\mathrm{b}]}}(x) = \int_0^x \mathsf{f}_{g_{l,n}^{[\mathrm{b}]}}(y)\mathsf{d}y = \int_0^x 2\,\mathsf{K}_0(2\sqrt{y})\,\mathsf{d}y$$
$$\overset{(a)}{=} \int_0^{2\sqrt{x}} z\,\mathsf{K}_0(z)\,\mathsf{d}z \overset{(b)}{=} 4\,x\int_0^1 y\,\mathsf{K}_0\big(2\sqrt{x}\,y\big)\,\mathsf{d}y$$
$$\overset{(c)}{=} 1 - 2\,\sqrt{x}\,\mathsf{K}_1(2\sqrt{x}),\ x \geq 0, \quad (52)$$

where step (a) used $2\sqrt{y} = z$, (b) $\frac{z}{2\sqrt{x}} = y$, and (c) used [33, eq. (6.561.8)]. Concavity of $\mathsf{F}_{g_{l,n}^{[\mathrm{b}]}}$ is shown by differentiating twice the CDF $\mathsf{F}_{g_{l,n}^{[\mathrm{b}]}}(x)$ and utilizing [32, eq. (10.29.3)]:

$$\frac{\mathsf{d}^2}{\mathsf{d}x^2}\mathsf{F}_{g_{l,n}^{[\mathrm{b}]}}(x) = \frac{\mathsf{d}}{\mathsf{d}x}\mathsf{f}_{g_{l,n}^{[\mathrm{b}]}}(x) = \frac{\mathsf{d}}{\mathsf{d}x}2\,\mathsf{K}_0\big(2\sqrt{x}\big) = -\frac{2\,\mathsf{K}_1(2\sqrt{x})}{\sqrt{x}} < 0, \quad (53)$$

since $\mathsf{K}_1(x) > 0, \forall x > 0$. Thus, $\mathsf{F}_{g_{l,n}^{[\mathrm{b}]}}$ is concave and Eq. (29) follows using the same reasoning as in Proposition 3.

REFERENCES

[1] G. Vannucci, A. Bletsas, and D. Leigh, "A software-defined radio system for backscatter sensor networks," *IEEE Trans. Wireless Commun.*, vol. 7, no. 6, pp. 2170–2179, Jun. 2008.

[2] J. A. Paradiso, K.-Y. Hsiao, and A. Y. Benbasat, "Tangible music interfaces using passive magnetic tags," in *Proc. ACM Conf. Human Factors Comput. Syst.*, Chicago, IL, USA, 2001, pp. 1–4.

[3] J. A. Paradiso, L. S. Pardue, K. Y. Hsiao, and A. Y. Benbasat, "Electromagnetic tagging for electronic music interfaces," *J. New Music Res.*, vol. 32, no. 4, pp. 395–409, Dec. 2003.

[4] K. Finkenzeller, *RFID Handbook: Fundamentals and Applications in Contactless Smart Cards and Identification*, 2nd ed. New York, NY, USA: Wiley, 2003.

[5] *EPC Radio-Frequency Identity Protocols, Class-1 Generation-2 UHF RFID Protocol for Communications at 860 MHZ–960 MHZ, Version 1.2.0*, EPC Global, 2008.

[6] A. Al-Fuqaha, M. Guizani, M. Mohammadi, M. Aledhari, and M. Ayyash, "Internet of Things: A survey on enabling technologies, protocols, and applications," *IEEE Commun. Surveys Tuts.*, vol. 17, no. 4, pp. 2347–2376, 4th Quart., 2015.

[7] P. N. Alevizos, "Intelligent scatter radio, RF harvesting analysis, and resource allocation for ultra-low-power Internet-of-Things," Ph.D. dissertation, School Elect. Comput. Eng., Tech. Univ. Crete, Chania, Greece, Dec. 2017.
[8] J. D. Griffin and G. D. Durgin, "Complete link budgets for backscatter-radio and RFID systems," *IEEE Antennas Propag. Mag.*, vol. 51, no. 2, pp. 11–25, Apr. 2009.
[9] A. Bletsas, S. Siachalou, and J. N. Sahalos, "Anti-collision backscatter sensor networks," *IEEE Trans. Wireless Commun.*, vol. 8, no. 10, pp. 5018–5029, Oct. 2009.
[10] J. D. Griffin and G. D. Durgin, "Link envelope correlation in the backscatter channel," *IEEE Commun. Lett.*, vol. 11, no. 9, pp. 735–737, Sep. 2007.
[11] J. D. Griffin and G. D. Durgin, "Gains for RF tags using multiple antennas," *IEEE Trans. Antennas Propag.*, vol. 56, no. 2, pp. 563–570, Mar. 2008.
[12] A. Bereketli and O. B. Akan, "Communication coverage in wireless passive sensor networks," *IEEE Commun. Lett.*, vol. 13, no. 2, pp. 133–135, Feb. 2009.
[13] K. Han and K. Huang, "Wirelessly powered backscatter communication networks: Modeling, coverage and capacity," *IEEE Trans. Wireless Commun.*, vol. 16, no. 4, pp. 2548–2561, Apr. 2017.
[14] J. Kimionis, A. Bletsas, and J. N. Sahalos, "Design and implementation of RFID systems with software defined radio," in *Proc. 6th Eur. Conf. Antennas Propag. (EUCAP)*, Mar. 2012, pp. 3464–3468.
[15] J. Kimionis, A. Bletsas, and J. N. Sahalos, "Bistatic backscatter radio for power-limited sensor networks," in *Proc. IEEE Global Commun. Conf. (GLOBECOM)*, Atlanta, GA, USA, Dec. 2013, pp. 353–358.
[16] J. Kimionis, A. Bletsas, and J. N. Sahalos, "Increased range bistatic scatter radio," *IEEE Trans. Commun.*, vol. 62, no. 3, pp. 1091–1104, Mar. 2014.
[17] P. N. Alevizos, N. Fasarakis-Hilliard, K. Tountas, N. Agadakos, N. Kargas, and A. Bletsas, "Channel coding for increased range bistatic backscatter radio: Experimental results," in *Proc. IEEE RFID Technol. Appl. Conf. (RFID-TA)*, Sep. 2014, pp. 38–43.
[18] P. Alevizos and A. Bletsas, "Noncoherent composite hypothesis testing receivers for extended range bistatic scatter radio WSNs," in *Proc. IEEE Int. Conf. Commun.*, London, U.K., Jun. 2015, pp. 4448–4453.
[19] N. Fasarakis-Hilliard, P. N. Alevizos, and A. Bletsas, "Coherent detection and channel coding for bistatic scatter radio sensor networking," *IEEE Trans. Commun.*, vol. 63, no. 5, pp. 1798–1810, May 2015.
[20] N. Kargas, F. Mavromatis, and A. Bletsas, "Fully-coherent reader with commodity SDR for Gen2 FM0 and computational RFID," *IEEE Wireless Commun. Lett.*, vol. 4, no. 6, pp. 617–620, Dec. 2015.
[21] P. N. Alevizos, A. Bletsas, and G. N. Karystinos, "Noncoherent short packet detection and decoding for scatter radio sensor networking," *IEEE Trans. Commun.*, vol. 65, no. 5, pp. 2128–2140, May 2017.
[22] E. Kampianakis, J. Kimionis, K. Tountas, C. Konstantopoulos, E. Koutroulis, and A. Bletsas, "Wireless environmental sensor networking with analog scatter radio and timer principles," *IEEE Sensors J.*, vol. 14, no. 10, pp. 3365–3376, Oct. 2014.
[23] S. N. Daskalakis, S. D. Assimonis, E. Kampianakis, and A. Bletsas, "Soil moisture wireless sensing with analog scatter radio, low power, ultra-low cost and extended communication ranges," in *Proc. IEEE Sensors*, Valencia, Spain, Nov. 2014, pp. 122–125.
[24] S. N. Daskalakis, S. D. Assimonis, E. Kampianakis, and A. Bletsas, "Soil moisture scatter radio networking with low power," *IEEE Trans. Microw. Theory Techn.*, vol. 64, no. 7, pp. 2338–2346, Jul. 2016.
[25] V. Liu, A. Parks, V. Talla, S. Gollakota, D. Wetherall, and J. R. Smith, "Ambient backscatter: Wireless communication out of thin air," in *Proc. ACM SIGCOMM*, Hong Kong, 2013, pp. 39–50.
[26] V. Iyer, V. Talla, B. Kellogg, S. Gollakota, and J. Smith, "Inter-technology backscatter: Towards Internet connectivity for implanted devices," in *Proc. ACM SIGCOMM Conf.*, 2016, pp. 356–369.
[27] G. Wang, F. Gao, R. Fan, and C. Tellambura, "Ambient backscatter communication systems: Detection and performance analysis," *IEEE Trans. Commun.*, vol. 64, no. 11, pp. 4836–4846, Nov. 2016.
[28] J. Qian, F. Gao, G. Wang, S. Jin, and H. Zhu, "Noncoherent detections for ambient backscatter system," *IEEE Trans. Wireless Commun.*, vol. 16, no. 3, pp. 1412–1422, Mar. 2017.
[29] A. Goldsmith, *Wireless Communications*. New York, NY, USA: Cambridge Univ. Press, 2005.
[30] A. Pappoulis and S. U. Pillai, *Probability, Random Variables and Stochastic Processes*, 4th ed. New York, NY, USA: McGraw-Hill, 2002.
[31] D. Tse and P. Viswanath, *Fundamentals of Wireless Communication*. New York, NY, USA: Cambridge Univ. Press, 2005.
[32] F. W. J. Olver, D. W. Lozier, R. F. Boisvert, and C. W. Clark, *NIST Handbook of Mathematical Functions*. New York, NY, USA: Cambridge Univ. Press, 2010.
[33] I. S. Gradshteyn and I. M. Ryzhik, *Table of Integrals, Series, and Products*, 7th ed. Amsterdam, The Netherlands: Elsevier, 2007.
[34] N. D. Chatzidiamantis, G. K. Karagiannidis, and D. S. Michalopoulos, "On the distribution of the sum of gamma-gamma variates and application in MIMO optical wireless systems," in *Proc. IEEE Global Commun. Conf. (Globecom)*, Honolulu, HI, USA, Nov. 2009, pp. 1–6.
[35] P. S. Bithas, N. C. Sagias, T. A. Tsiftsis, and G. K. Karagiannidis, "Distributions involving correlated generalized gamma variables," in *Proc. Int. Conf. Appl. Stochastic Models Data Anal. (ASMDA)*, Crete, Greece, 2007. [Online]. Available: http://www.asmda.com//CDasmda2007a/conf_papers.html
[36] J. G. Proakis and M. Salehi, *Digital Communications*, 5th ed. New York, NY, USA: McGraw-Hill, 2007.
[37] G. D. Durgin, "RF thermoelectric generation for passive RFID," in *Proc. IEEE Int. Conf. RFID*, Orlando, FL, USA, May 2016, pp. 1–8.
[38] J. M. Romero-Jerez and A. J. Goldsmith, "Receive antenna array strategies in fading and interference: An outage probability comparison," *IEEE Trans. Wireless Commun.*, vol. 7, no. 3, pp. 920–932, Mar. 2008.
[39] K. Tountas, "Performance analysis, middleware and hardware for bistatic, ultra-low power scatter radio networks," M.S. thesis, School Elect. Comput. Eng., Tech. Univ. Crete, Chania, Greece, Jul. 2016.
[40] L. Zheng and D. N. C. Tse, "Diversity and multiplexing: A fundamental tradeoff in multiple antenna channels," *IEEE Trans. Inf. Theory*, vol. 49, no. 5, pp. 1073–1096, May 2003.
[41] B. C. Levy, *Principles Signal Detection Parameter Estimation*. New York, NY, USA: Springer, 2008.

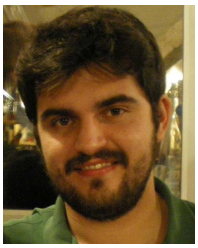

Panos N. Alevizos (S'14) received the Diploma and M.Sc. degrees in electronic and computer engineering and the Ph.D. degree in electrical and computer engineering from the Technical University of Crete, Greece, in 2012, 2014, and 2017, respectively. His research interests include communications theory, probabilistic inference and signal processing for wireless communications and networking, with emphasis on backscatter radio, RFIDs, and massive MIMO. He was a co-recipient of the IEEE ICASSP 2015 Best Student Paper Award.

Konstantinos Tountas received the Diploma and M.Sc. degrees in electronic and computer engineering from the Technical University of Crete, Greece, in 2014 and 2016, respectively. He is currently pursuing the Ph.D. degree with the Department of Computer and Electrical Engineering and Computer Science, Florida Atlantic University, Boca Raton, FL, USA. His research interests span the areas of signal processing, machine learning, and localization, software-defined wireless communications, and underwater acoustic communications.

Aggelos Bletsas (S'03–M'05–SM'14) received the Diploma degree (Hons.) in electrical and computer engineering from the Aristotle University of Thessaloniki, Greece, in 1998, and the S.M. and Ph.D. degrees from the Massachusetts Institute of Technology, Cambridge, MA, USA, in 2001 and 2005, respectively.

He currently serves as an Associate Professor with the School of Electrical and Computer Engineering, Technical University of Crete, Greece. His research interests span the broad area of scalable wireless communications and sensors networking.

Dr. Bletsas was a co-recipient of the IEEE Communications Society 2008 Marconi Prize Paper Award in Wireless Communications, the Best Paper Distinction at ISWCS 2009, Siena, Italy, the Second Best Student Paper Award at the IEEE RFID-TA 2011, Sitges, Spain, the Best Paper Distinction at the IEEE Sensors 2013, Baltimore, MD, USA, the Best Student Paper Award at the IEEE ICASSP 2015, Brisbane, QLD, Australia, and the Best Student Paper Award at the IEEE RFID-TA 2017, Warsaw, Poland.